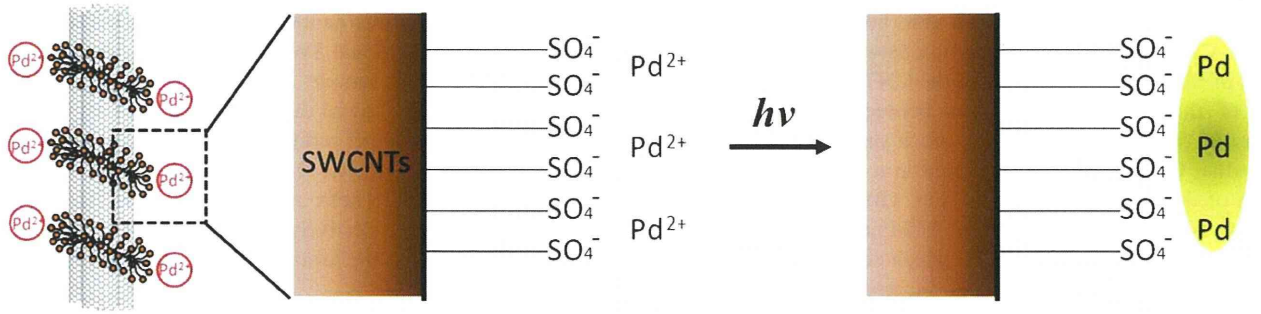

Scheme 2 Photoreduction of Pd on the surface of the SWCNTs.

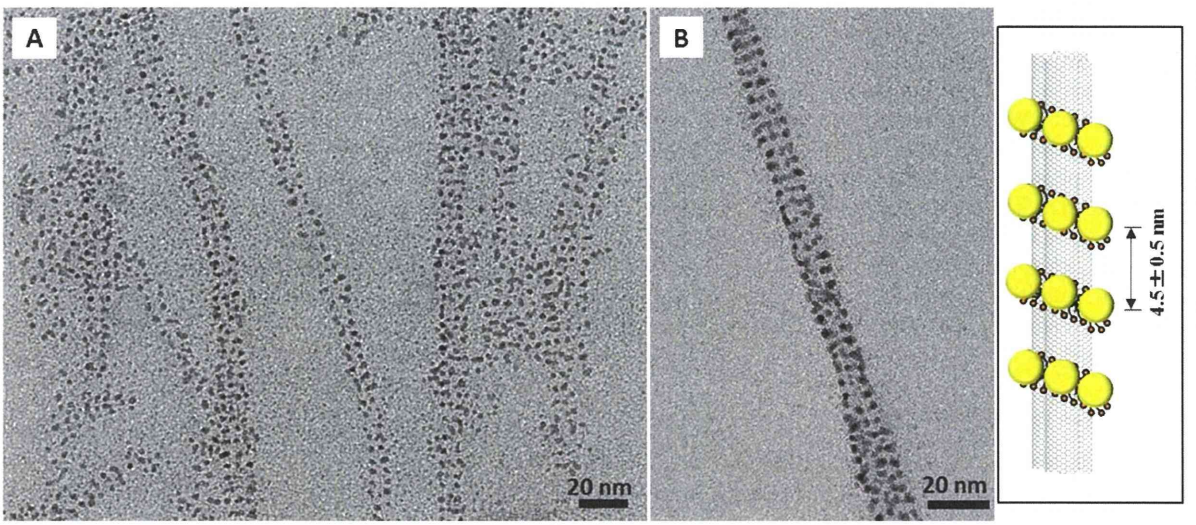

Fig. 3 TEM image of (A) Pd NPs arranged on the SDS-functionalized SWCNTs. High resolution TEM image (B) showing how the Pd NPs form a unique helical nanostructure wrapped around a nanotube.

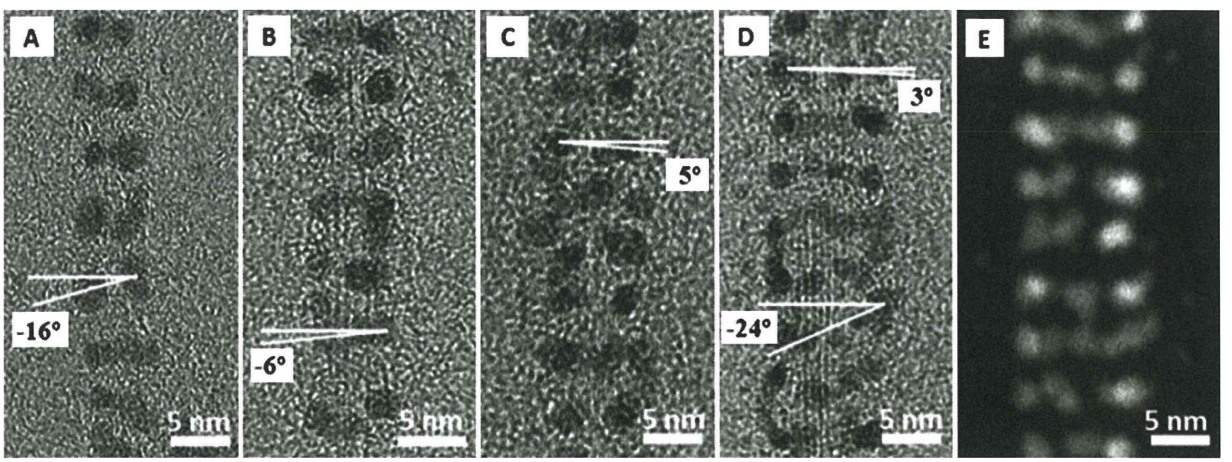

Fig. 4 Different helical arrangements of Pd NPs on SDS-functionalized SWCNTs: (A) a right-hand helix with a helix angle of −16°; (B) a right-hand helix with a helix angle of −6°; (C) a left-hand helix with a helix angle of 5°; and (D) a left-hand helix with a helix angle of 3°, and a right helix with a tilt angle of −24°. (E) A dark field STEM image of Pd NPs wrapped around a small bundle of SWCNTs.

Photoreduction has been widely used to fabricate metal NPs and nanostructures.[47–50] In this study, SDS acted as a template to absorb Pd(II) onto the surface of the SWCNTs. Pd was then reduced by a photoreduction reaction involving hydrated electrons formed in the radiolysis of water molecules in the solvent.[51–53]

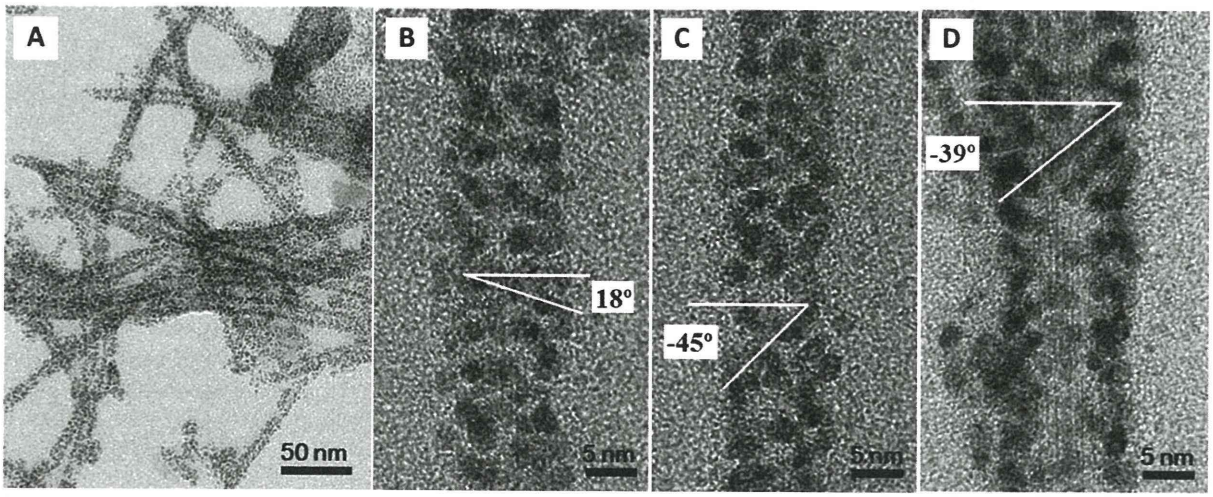

Fig. 5 High resolution TEM images of (A) Pd NPs that have formed a supramolecular self-assembly on SDS-functionalized SWCNTs. (B) Left-handed helices with a helix angle of 18°. (C and D) Right-handed helices with helix angles of −45° and −39°, respectively.

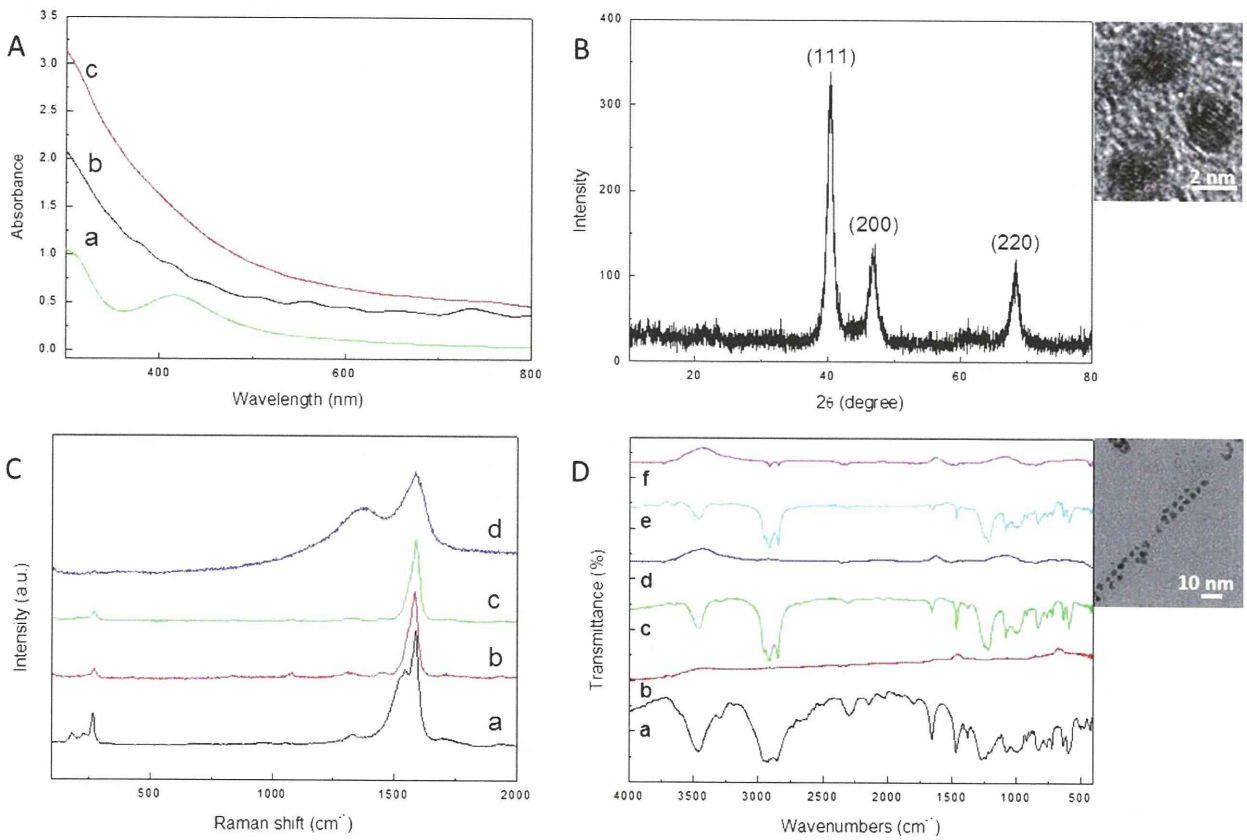

Fig. 6 (A) UV-Vis absorption spectra of (a) $PdCl_2$ aqueous solution, (b) SDS-functionalized SWCNTs aqueous dispersion, and (c) aqueous dispersion of SWCNTs with deposited Pd NPs. (B) XRD profile of Pd NPs deposited on SWCNTs. The inset shows a typical TEM image of Pd NPs. (C) Raman spectra of (a) pristine SWCNTs, (b) SDS-functionalized SWCNTs, (c) Pd(II) ion-adsorbed SWCNTs, and (d) Pd NPs-decorated SWCNTs. (D) Diffuse reflectance infrared spectrum of (a) SDS, (b) the original SWCNTs, (c) SDS-functionalized SWCNTs, (d) SDS-functionalized SWCNTs after alcohol washing, (e) SWCNTs with deposited Pd NPs, and (f) SWCNTs with deposited Pd NPs after alcohol washing. The inset shows a typical TEM image of Pd NPs deposited on SWCNTs after alcohol washing.

$$H_2O \xrightarrow{h\nu} H^+ + e_{aq}^- + OH \quad (1)$$

$$Pd^{2+} + 2e_{aq}^- \longrightarrow Pd \quad (2)$$

This reaction mechanism suggests that it has potential to be applied to synthesize many other metal NPs on the SDS-functionalized SWCNTs.

XRD pattern (Fig. 6B) of the Pd NPs on the SDS-functionalized SWCNTs revealed three diffraction peaks at $2\theta = 40.3$, 46.7 and 68.4°, which could be assigned to the (111), (200) and (220) planes, respectively, of the polycrystalline Pd NPs.[54] The lattice parameters of the Pd NPs evaluated from the XRD measurement were 0.388 nm, which is in agreement with the standard value (0.389 nm).[55] Different crystal facets were clearly visible in the high-resolution TEM image (inset Fig. 6B) of typical Pd NPs deposited on the SDS-functionalized SWCNTs.

Fig. 6C shows Raman spectra of SWCNTs and Pd NPs decorated SWCNTs. The pristine SWCNTs show a strong G band at 1587 and 1545 cm^{-1}. The D band feature of pristine SWCNTs is very weak, and appears at 1330 cm^{-1} (Fig. 6C-a). The radial breathing mode (RBM) frequency of pristine SWCNTs is found to be 268, 228 and 181 cm^{-1}. It indicates that pristine SWCNTs are mainly a mixture with such tubes having diameters of 0.84, 0.98 and 1.24 nm.[56,57] When the surface of SWCNTs was functionalized with SDS molecules, the intensity of Raman absorption was decreased, and the G band was shifted to 1584 cm^{-1} (Fig. 6C-b). It indicates that the surface-adsorbed SDS molecules may influence the Raman vibration feature of SWCNTs by forming the hydrophobic interaction. Fig. 6C-c shows a Raman spectrum of Pd(II) ion-adsorbed SWCNTs before UV light irradiation. The Raman feature is the same to that of SDS-functionalized SWCNTs. Finally, Fig. 6C-d is the Raman spectrum of SWCNTs after Pd NPs arranged on their wall. Interestingly, we found that this Raman spectrum is changed from others. The G band is greatly broadened and centered at 1585 cm^{-1}. The D band also shows a strong and broad absorption at 1368 cm^{-1}. The RBM mode at the frequency range of 100–300 cm^{-1} almost disappeared. The Raman spectrum suggests that defects are mass produced on the SWCNT's wall after Pd reduced and deposited on the tube. Such surface defects may be generated by the radical oxidation corrosion under the 254 nm UV light irradiation.

The interaction between the SDS molecules and SWCNTs was characterized by diffuse reflectance FTIR (Fig. 6D-a). The original SDS showed absorption peaks at 2957, 2928 and 2853 cm^{-1} (C–H stretching), 1468 and 1377 cm^{-1} (C–H bending), and 1267, 1236 and 1206 cm^{-1} ($-OSO_3-$ stretching).[58,59] A prominent absorption band was also observed at 3460 cm^{-1} for the O–H stretching vibration of absorbed water. The SWCNTs produced no obvious IR absorption bands between 4000 and 1000 cm^{-1} (Fig. 6D-b). When SDS was adsorbed on the SWCNTs (Fig. 6D-c), the IR absorption peaks of SDS shifted to slightly lower frequency as follows: C–H stretching at 2955, 2918, 2845 cm^{-1}; C–H bending at 1467 and 1376 cm^{-1}; and $-OSO_3-$ stretching at 1246, 1217, 1082 cm^{-1}. These shifts may be attributed to hydrophobic interactions between SDS and the SWCNTs which we have also observed in the Raman spectra (Fig. 6C). These peaks disappeared after washing with alcohol and filtration (Fig. 6D-d), which proves that SDS molecules can be easily removed from the surface of the SWCNTs because the interactions are only weak van der Waals interactions. With Pd NPs on the SDS the IR spectrum (Fig. 6D-e) was very similar to that of the SDS-functionalized SWCNTs (Fig. 6D-c). After washing and filtration of these SWCNTs, the IR absorption peaks of SDS (Fig. 6D-f) decreased to a very low level, which was approximately equal to that of the CO_2 peak at 2355 cm^{-1}. This indicates that SDS was almost completely removed from the SWCNTs. The inset of Fig. 6D shows a typical TEM image of Pd NPs supported on SWCNTs after alcohol washing. Although some Pd NPs seem to be removed from SWCNTs accompanied with the removing of SDS, most of Pd NPs were stably supported on the surface of SWCNTs. The removal of SDS is an advantage of this soft template method, and is important as SDS could degrade the performance of the Pd NP coated SWCNTs.

Conclusions

A simple chemical solution approach was developed to site-selectively deposit Pd NPs on the surface of SDS-functionalized SWCNTs with sub-10 nm diameter. The SDS formed a helical supramolecular self-assembly around the SWCNTs. This provided functional sites for electrostatic adsorption and immobilization of Pd(II) ions, which could then be reduced to Pd NPs. The Pd NPs formed a similar ordered helical nanostructure on the surface of the SWCNTs. Increasing the concentration of Pd(II) ions resulted in higher density deposition of Pd NPs on the surface of the SWCNTs. This is important to enhance the catalytic performance for potential applications. Because the electrostatic interaction between the negatively charged group of SDS and the positively charged metal ion is non-selective, this approach could be applied to other metal NPs and/or quantum dots.

Acknowledgements

This research was partly supported by a Scientific Research Grant and Grant-in-Aid for Cooperative Research Project of Advanced Materials Development and Integration of Novel Structured Metallic and Inorganic Materials from the Ministry of Education, Culture, Sports, Science and Technology of Japan.

Notes and references

1 R. H. Baughman, A. A. Zakhidov and W. A. de Heer, *Science*, 2002, **297**, 787.
2 P. Avouris, Z. Chen and V. Perebeinos, *Nat. Nanotechnol.*, 2007, **2**, 605.
3 P. M. Ajayan and J. M. Tour, *Nature*, 2007, **447**, 1066.
4 N. Narita, Y. Kobayashi, H. Nakamura, K. Maeda, A. Ishihara, T. Mizoguchi, Y. Usui, K. Aoki, M. Simizu, H. Kato, H. Ozawa, N. Udagawa, M. Endo, N. Takahashi and N. Saito, *Nano Lett.*, 2009, **9**, 1406.
5 G. G. Wildgoose, C. E. Banks and R. G. Compton, *Small*, 2006, **2**, 182.
6 B. Yoon and C. M. Wai, *J. Am. Chem. Soc.*, 2005, **127**, 17174.
7 M. Sanles-Sobrido, M. A. Correa-Duarte, S. Carregal-Romero, B. Rodríguez-González, R. A. Álvarez-Puebla, P. Hervés and L. M. Liz-Marzán, *Chem. Mater.*, 2009, **21**, 1531.
8 M. Kaempgen, M. Lebert, N. Nicoloso and S. Roth, *Appl. Phys. Lett.*, 2008, **92**, 094103.
9 V. Selvaraj and M. Alagar, *Nanotechnology*, 2008, **19**, 045504.

10 Y. Lu, J. Li, J. Han, H.-T. Ng, C. Binder, C. Partridge and M. Meyyappan, *Chem. Phys. Lett.*, 2004, **391**, 344.
11 P. C. P. Watts, S. J. Henley, E. Mendoza, S. R. P. Silva, J. K. Irvineand and E. T. McAdams, *Nanotechnology*, 2007, **18**, 205502.
12 K. Jiang, A. Eitan, L. S. Schadler, P. M. Ajayan, R. W. Siegel, N. Grobert, M. Mayne, M. Reyes-Reyes, H. Terrones and M. Terrones, *Nano Lett.*, 2003, **3**, 275.
13 N. Mackiewicz, G. Surendran, H. Remita, B. Keita, G. Zhang, L. Nadjo, A. Hagège, E. Doris and C. Mioskowski, *J. Am. Chem. Soc.*, 2008, **130**, 8110.
14 L. Han, W. Wu, F. L. Kirk, J. Luo, M. M. Maye, N. N. Kariuki, Y. Lin, C. Wang and C.-J. Zhong, *Langmuir*, 2004, **20**, 6019.
15 X. Hu, T. Wang, X. Qu and S. Dong, *J. Phys. Chem. B*, 2006, **110**, 853.
16 C. Gao, W. Li, Y. Z. Jin and H. Kong, *Nanotechnology*, 2006, **17**, 2882.
17 M. A. Correa-Duarte, N. Sobal, L. M. Liz-Marzán and M. Giersig, *Adv. Mater.*, 2004, **16**, 23.
18 M. A. Correa-Duarte, J. Pérez-Juste, A. Sánchez-Iglesias, M. Giersig and L. M. Liz-Marzán, *Angew. Chem., Int. Ed.*, 2005, **44**, 4375.
19 T. M. Day, P. R. Unwin, N. R. Wilson and J. V. Macpherson, *J. Am. Chem. Soc.*, 2005, **127**, 10639.
20 D. R. Kauffman and A. Star, *Nano Lett.*, 2007, **7**, 1863.
21 X.-R. Ye, Y. Lin, C. Wang, M. H. Engelhard, Y. Wang and C. M. Wai, *J. Mater. Chem.*, 2004, **14**, 908.
22 A. Felten, C. Bittencourt, J.-F. Colomer, G. Van Tendeloo and J.-J. Pireaux, *Carbon*, 2007, **45**, 110.
23 M. Zheng, A. Jagota, E. D. Semke, B. A. Diner, R. S. McLean, S. R. Lustig, R. E. Richardson and N. G. Tassi, *Nat. Mater.*, 2003, **2**, 338.
24 A. Nish, J.-Y. Hwang, J. Doig and R. J. Nicholas, *Nat. Nanotechnol.*, 2007, **2**, 640.
25 C. Thauvin, S. Rickling, P. Schultz, H. Celia, S. Meunier and C. Mioskowski, *Nat. Nanotechnol.*, 2008, **3**, 743.
26 S.-Y. Ju, J. Doll, I. Sharma and F. Papadimitrakopoulos, *Nat. Nanotechnol.*, 2008, **3**, 356.
27 S.-Y. Ju, W. P. Kopcha and F. Papadimitrakopoulos, *Science*, 2009, **323**, 1319.
28 X. Tu, S. Manohar, A. Jagota and M. Zheng, *Nature*, 2009, **460**, 250.
29 D. Wang, Z. Li and L. Chen, *J. Am. Chem. Soc.*, 2006, **128**, 15078.
30 C. Y. Li, L. Y. Li, W. W. Cai, S. L. Kodjie and K. K. Tenneti, *Adv. Mater.*, 2005, **17**, 1198.
31 L. Li, Y. Yang, G. Yang, X. Chen, B. S. Hsiao, B. Chu, J. E. Spanier and C. Y. Li, *Nano Lett.*, 2006, **6**, 1007.
32 L. Li, C. Y. Li and C. Ni, *J. Am. Chem. Soc.*, 2006, **128**, 1692.
33 B. Li, L. Li, B. Wang and C. Y. Li, *Nat. Nanotechnol.*, 2009, **4**, 358.
34 W. Wenseleers, I. I. Vlasov, E. Goovaerts, E. D. Obraztsoca, A. S. Lobach and A. Bouwen, *Adv. Funct. Mater.*, 2004, **14**, 1105.
35 M. C. Hersam, *Nat. Nanotechnol.*, 2008, **3**, 387.
36 M. Burghard, G. Duesberg, G. Philipp, J. Muster and S. Roth, *Adv. Mater.*, 1998, **10**, 584.
37 M. J. O'Connell, S. M. Bachilo, C. B. Huffman, V. C. Moore, M. S. Strano, E. H. Haroz, K. L. Rialon, P. J. Boul, W. H. Noon, C. Kittrell, J. Ma, R. H. Hauge, R. B. Weisman and R. E. Smalley, *Science*, 2002, **297**, 593.
38 C. Richard, F. Balavoine, P. Schultz, T. W. Ebbesen and C. Mioskowski, *Science*, 2003, **300**, 775.
39 Z. Tan, H. Abe, M. Naito and S. Ohara, *Chem. Commun.*, 2010, **46**, 4363.
40 Y. Hatakeyama, M. Umetsu, S. Ohara, F. Kawadai, S. Takami, T. Naka and T. Adschiri, *Adv. Mater.*, 2008, **20**, 1122.
41 Y.-H. Chen, H.-H. Hung and M. H. Huang, *J. Am. Chem. Soc.*, 2009, **131**, 9114.
42 H. Liu, T. Jiang, B. Han, S. Liang and Y. Zhou, *Science*, 2009, **326**, 1250.
43 H. Xu, H. Abe, M. Naito, H. Ichikawa, Y. Fukumori and S. Endoh, *J. Ceram. Soc. Jpn.*, 2008, **116**, 965.
44 Z. Tan, H. Xu, H. Abe, M. Naito and S. Ohara, *J. Nanosci. Nanotechnol.*, 2010, **10**, 3978.
45 S. M. Bachilo, M. S. Strano, C. Kittrell, R. H. Hauge, R. E. Smalley and R. B. Weisman, *Science*, 2002, **298**, 2361.
46 L. I. Elding and L. F. Olsson, *J. Phys. Chem.*, 1978, **82**, 69.
47 Y. Zhou, S. H. Yu, C. Y. Wang, X. G. Li, Y. R. Zhu and Z. Y. Chen, *Adv. Mater.*, 1999, **11**, 850.
48 M. Maillard, P. Huang and L. Brus, *Nano Lett.*, 2003, **3**, 1611.
49 A. S. Korchev, M. J. Bozack, B. L. Slaten and G. Mills, *J. Am. Chem. Soc.*, 2004, **126**, 10.
50 L. Berti, A. Alessandrini and P. Facci, *J. Am. Chem. Soc.*, 2005, **127**, 11216.
51 A. Henglein, M. Gutierrez, E. Janata and B. G. Ershov, *J. Phys. Chem.*, 1992, **96**, 4598.
52 Q. Fang, G. He, W. P. Cai, J. Y. Zhang and I. W. Boyd, *Appl. Surf. Sci.*, 2004, **226**, 7.
53 T. Redjala, G. Apostolecu, P. Beaunier, M. Mostafavi, A. Etcheberry, D. Uzio, C. Thomazeau and H. Remita, *New J. Chem.*, 2008, **32**, 1403.
54 B. Xue, P. Chen, Q. Hong, J. Lin and K. L. Tan, *J. Mater. Chem.*, 2001, **11**, 2378.
55 M. J. Mehl and D. A. Papaconstantopoulos, *Phys. Rev. B: Condens. Matter Mater. Phys.*, 1996, **54**, 4519.
56 A. M. Rao, E. Richter, S. Bandow, B. Chase, P. C. Eklund, K. A. Williams, S. Fang, K. R. Subbaswamy, M. Menon, A. Thess, R. E. Smalley, G. Dresselhaus and M. S. Dresselhaus, *Science*, 1997, **275**, 187.
57 M. S. Dresselhaus and P. C. Eklund, *Adv. Phys.*, 2000, **49**, 705.
58 K. D. Dobson, A. D. Roddick-Lanzilotta and A. J. McQuillan, *Vib. Spectrosc.*, 2000, **24**, 287.
59 R. P. Sperline, *Langmuir*, 1997, **13**, 3715.

Advanced Powder Technology 22 (2011) 559–565

Contents lists available at ScienceDirect

Advanced Powder Technology

journal homepage: www.elsevier.com/locate/apt

Review paper

Fabrication of Pd–DNA and Pd–CNT hybrid nanostructures for hydrogen sensors

Satoshi Ohara [a,*], Yoshiharu Hatakeyama [b], Mitsuo Umetsu [c], Zhenquan Tan [a], Tadafumi Adschiri [b,d]

[a] Joining and Welding Research Institute, Osaka University, 11-1 Mihogaoka, Ibaraki, Osaka 567-0047, Japan
[b] Institute of Multidisciplinary Research for Advanced Materials, Tohoku University, 2-1-1 Katahira, Aoba-ku, Sendai, Miyagi 980-8577, Japan
[c] Department of Biomolecular Engineering, Graduate School of Engineering, Tohoku University, 6-6-11 Aoba, Aramaki, Aoba-ku, Sendai 980-8579, Japan
[d] Advanced Institute for Materials Research, Tohoku University, 2-1-1 Katahira, Aoba-ku, Sendai, Miyagi 980-8577, Japan

ARTICLE INFO

Article history:
Received 8 March 2011
Received in revised form 27 April 2011
Accepted 13 May 2011
Available online 26 May 2011

Keywords:
Palladium
DNA
CNT
Hybrid nanostructures
Hydrogen sensors

ABSTRACT

This review reports fabrication methods for ordered metallic nanostructures such as nanowires and nanoparticles based on deoxyribonucleic acid (DNA) templates. The phosphate groups in DNA are negatively charged; consequently, the DNA conformation may mineralize metals, e.g., palladium (Pd) at a relatively high metal concentration. We successfully form unique spherically shaped moss-like hybrid Pd nanoparticles using the small compacted globular state of DNA by controlling the reductive reaction. Pd can absorb hydrogen to become PdH_x, and hydrogen storage increases the electrical resistance and volume of Pd materials. Hence, the use of this material is attracting growing interest as a reliable, cheap, ultracompact, and safe hydrogen sensor. Pd–DNA hybrid nanoparticles can be used as highly sensitive hydrogen sensors, which exhibit a switch response that depends on the volume expansion in a cyclic atmosphere exchange. This paper also shows the fabrications of Pd–carbon nanotube (CNT) hybrid nanostructures.

Contents

1. Introduction

The 20th century was the so-called age of new material synthesis [1]. Syntheses of new substances were essential to attain new material properties. However, recent material R&D has focused on controlling material functions via the material structure. One example is nanotechnology. To control the material structure, the process is more important than the synthesis.

For example, the size and shape of nanoparticles significantly depend on the operating conditions during the crystallization process. Some semiconductor materials show a strong photo-luminescence, and the particle size can control the wavelength (quantum size effect). Consequently, changing the nanoparticle size of quantum dots (QDs) results in a wide range of color using the same excitation wavelength for CdSe, CdTe, CdS, etc. [2]. The next stage of the nanotechnology will be to assemble nanomaterials because this is a foreseeable future target in various industries. In device production by assembling structured materials, fabrication is a key technology. Thus, science and technology for materials is shifting from synthesis towards processing and fabrication.

Nanobiotechnology has great potential in the fabrication of nanostructured materials where specific interactions between molecules of deoxyribonucleic acid (DNA) or peptide are used to create assemblies of multi-component nanomaterials or nanoblocks, such as QDs, nanocrystals, biomaterials, and bio-reactive nanomaterials. Controlling the assembly of various bio-molecules and nanoblocks will be crucial in the fabrication of multi-component

* Corresponding author.
E-mail address: ohara@jwri.osaka-u.ac.jp (S. Ohara).

0921-8831/$ - see front matter © 2011 The Society of Powder Technology Japan. Published by Elsevier B.V. and The Society of Powder Technology Japan. All rights reserved.
doi:10.1016/j.apt.2011.05.006

and multi-structured materials. Furthermore, if the assembly of the nanostructured materials can be controlled by manipulating the solution environment, the material can dynamically alter its structure.

This paper reports fabrication methods for ordered metallic nanostructures such as nanowires and nanoparticles based on the use of DNA templates. We successfully form unique spherically shaped moss-like hybrid palladium (Pd) nanoparticles using the small compacted globular state of DNA to control the reductive reaction [3]. Then we utilize Pd–DNA hybrid nanoparticles as highly sensitive hydrogen sensors. These sensors exhibit a hydrogen-actuated switch, i.e., an on–off current response that depends on the volume expansion in a cyclic atmosphere exchange [3,4]. This paper also shows the fabrication of Pd–carbon nanotube (CNT) hybrid nanostructures [5].

2. Pd–DNA hybrid nanostructures

DNA is an appropriate biopolymer template to construct defined inorganic materials. Highly selective base-pairing interactions between complementary single-strand DNA chains have been used for nanoassemblies. For instance, gold nanoparticles with single-strand DNA molecules immobilized on a surface can reversibly assemble [6,7], and a building-up process using complementary DNA strands enables artificial nanostructured templates to be created for these nanoparticle assemblies [8–10]. Additionally, native double-helical DNA directly interacts with metal ions and their complexes as illustrated in Fig. 1. The binding of metal ions or complexes to DNA has been utilized for DNA metallization to form nanowires, which can connect electronic components into nano-electronic circuits. Several metals such as Au [11,12], Ag [13,14], Pd [15–17], Pt [17], and Cu [18] have been deposited on DNA chains, and the electrical conductivities of some metal-deposited DNA nanowires have been measured [13,16].

Here we fabricate metal-DNA hybrid nanostructures via a combination of metallization and DNA compaction. DNA strands possess binding sites for metal ions and cation molecules in their nucleoside bases and backbone. Direct binding to DNA can cause a morphological change in the DNA strands; metal complexes can shorten DNA strands [17,19] while multivalent cation molecules can cause a transition from a coiled to a compact structure [20,21]. We compacted λ-DNA using Pd(II) complexes and subsequently reduced the Pd(II)-coordinated DNA strands to create a unique spherically shaped moss-like hybrid structure.

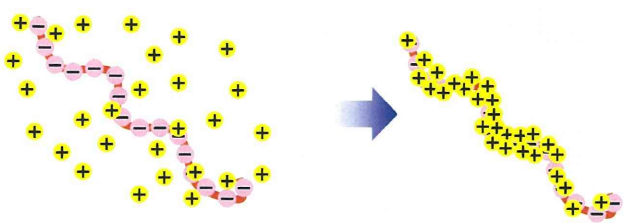

Fig. 1. Schematic illustration of the interaction of DNA and metal ions.

Fig. 2 shows fluorescence images for YOYO-stained λ-DNA in Pd(II) solutions with various concentrations prepared from Na_2PdCl_4. Without Pd(II), λ-DNA at a bp concentration of 225 μM forms a strip-shaped conformation, confirming the dominant coil conformation in a Pd-free solution (Fig. 2a). The coil conformation is also observed when the Pd(II) concentration is twice that of the bps Fig. 2. However, when the Pd(II) concentration is five times higher than that of bps, λ-DNA is compacted into a small spherical conformation (Fig. 2c), indicating that individual DNA molecules are compacted into a spherical globule state by interacting with Pd(II) complexes.

Various multivalent cation molecules/complexes have been reported to cause a transition from a coiled conformation to a small compact structure [20,21]. The positively charged multivalent molecules interact with the negatively charged phosphate groups in the DNA backbone, and the neutralization of the DNA results in compaction [22,23]. Furthermore, recent studies have reported that binding metal complexes to nucleoside bases shrivels the DNA strands [17,19]. The interaction of divalent metal cations with DNA has been investigated using a variety of techniques. Raman spectroscopy has demonstrated that the Pd(II) ion prepared from a $PdCl_2$ solution interacts with the N7 position of purine rings [24]. In general, Pd(II) exists as $[PdCl_4]^{2-}$ and $[PdCl_3]^-$ in solution, which tend to be hydrated into $PdCl_2(H_2O)_2$ complexes [17].

In the case of Pt(II) complexes, $PtCl_2(H_2O)_2$ complexes interact with the N7 positions in DNA bases, and the H_2O molecules in $PtCl_2(H_2O)_2$ are replaced by the N7 positions in guanine bases [25,26]. Therefore, our results suggest that Pd(II) complexes such as $PdCl_2(H_2O)_2$ induce compaction of DNA by binding to nucleoside bases. In previous studies, introducing organic molecules such as spermidine causes folding into compacted states for metallization in the globule structure format [14]. Our results show that Pd(II) complexes can cause compaction of λ-DNA without globule-inducing organic molecules.

To fabricate a Pd–DNA hybrid nanostructures, a Pd(II) solution prepared from Na_2PdCl_4 is reduced by ascorbic acid or $NaBH_4$ in the presence of λ-DNA (bp concentration = 225 μM). In the case of ascorbic acid, reduction of a low-concentration Pd(II) solution (450 μM) forms a Pd–DNA hybrid nanowire (Fig. 3). Pd nanoparticles with an average size of about 5 nm are assembled into strips, implying Pd(II) condenses onto DNA, leading to nucleus formation from condensed Pd(II). Furthermore, reduction at a high Pd(II) concentration (1.13 mM) causes λ-DNA to be compacted, resulting in spherical moss-like Pd–DNA hybrid nanoparticles (Fig. 4). Three to five nanometers Pd primary nanoparticles are formed in the very homogeneous moss-like hybrid nanostructures (Fig. 5). The compacted structure of λ-DNA serves as a template for Pd primary nanoparticle assembly through the binding of Pd to the nucleoside bases. On the other hand, in the case of $NaBH_4$, the reduction of a high-concentration Pd(II) solution (2.25 mM) forms a Pd–DNA hybrid nanonecklace where the hybrid nanoparticles are connected (Fig. 6).

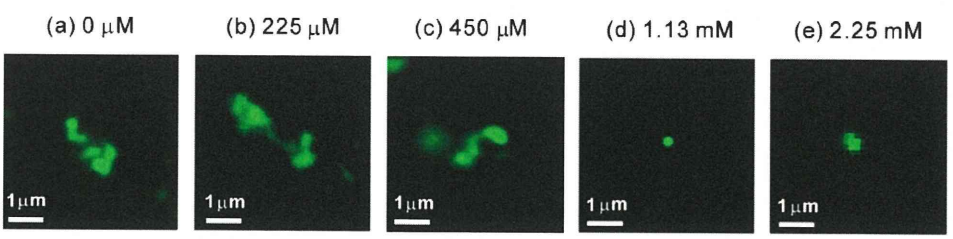

Fig. 2. Fluorescent images of YOYO-dyed λ-DNA in a 10 mM Tris-HCl solution at pH 8.0 and various Pd(II) concentrations. Data reproduced from Hatakeyama et al. [3].

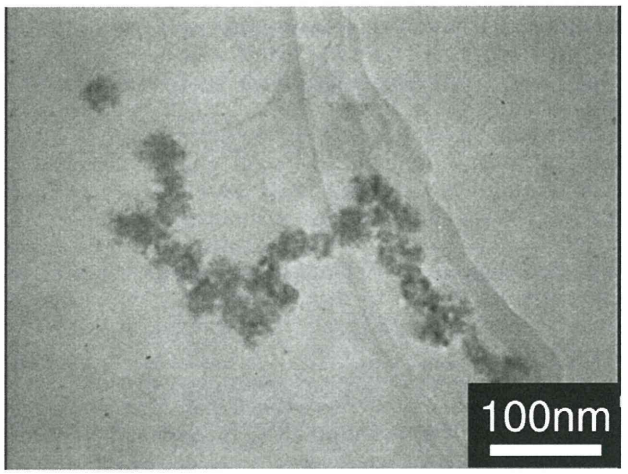

Fig. 3. TEM image of Pd(II) nanoparticles synthesized by ascorbic acid reduction in the presence of λ-DNA. Pd–DNA hybrid nanowire is synthesized when the concentration of applied Pd(II) ions is 450 μM.

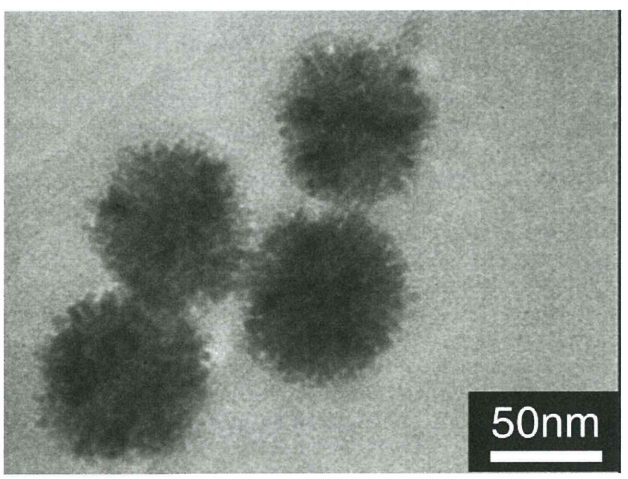

Fig. 4. TEM image of Pd(II) nanoparticles synthesized by ascorbic acid reduction in the presence of λ-DNA. Pd–DNA hybrid nanoparticles are formed when the concentration of applied Pd(II) ions is 1.13 mM.

Now let us compare reductions using $NaBH_4$ and ascorbic acid. The compacted DNA structure cannot be adequately utilized as a template in the reduction by $NaBH_4$. Yoshikawa et al. have reported that ascorbic acid induces a conformation change in partially compacted DNA structures [27]. In contrast, our research has found that small moss-like Pd–DNA hybrid nanoparticles are formed when the ascorbic acid concentration in the reduction of Pd(II) complexes increase. This result suggests that ascorbic acid

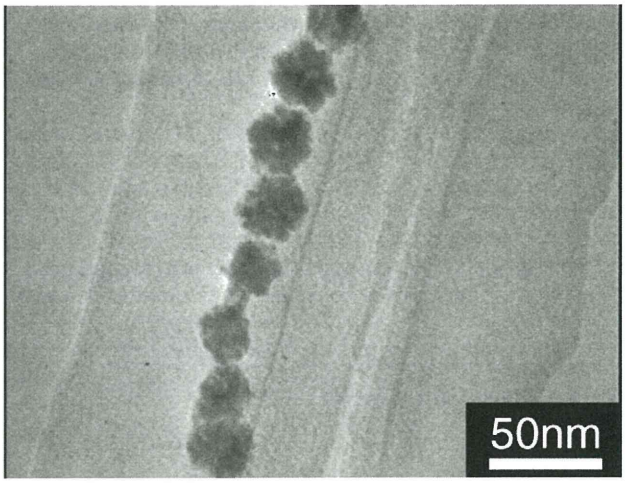

Fig. 6. TEM image of Pd(II) nanoparticles synthesized by $NaBH_4$ reduction in the presence of λ-DNA. Pd–DNA hybrid nanonecklace is obtained when the concentration of applied Pd(II) ions is 2.25 mM.

functions as both a reducing reagent and a stabilizing additive for the compacted DNA structure.

Fig. 7 schematically illustrates the formation of Pd–DNA hybrid nanostructures. When the Pd(II) is more than five times higher than the bp concentration, λ-DNA is compacted into a spherical globule conformation. Pd(II)–DNA complexes are chemically reduced to form Pd primary nanoparticles from the Pd(II) ions in the compacted DNA conformations. Consequently, the Pd nanoparticles are assembled in a moss-like manner on the DNA template.

The reducing reagent is critical for the homogeneous formation of moss-like Pd–DNA clusters; $NaBH_4$ partly denatures compacted DNA, and a hybrid nanonecklace structure may be formed as an intermediate. In contrast, ascorbic acid does not induce denaturation because it stabilizes compacted DNA. The transformations of λ-DNA into a compacted conformation is mainly caused by the interaction of Pd(II) with DNA causes, but is not attributable to the reduction of Pd(II). The interaction of ascorbic acid with DNA maintains the compacted DNA conformation even after the reduction of Pd(II). Hence, Pd nanoparticles synthesized with compacted DNA may bind some Pd with DNA to stabilize the moss-like Pd–DNA assemblies.

3. Hydrogen-sensing properties

Due to the real and perceived hazards of hydrogen fuel, its production and storage require extensive safety precautions. Currently, commercial hydrogen detectors are not widely used because they are bulky, expensive, and potentially dangerous. However, recent work has developed promising technologies to satisfy future demands such as reliable, cheap, compact, and safe

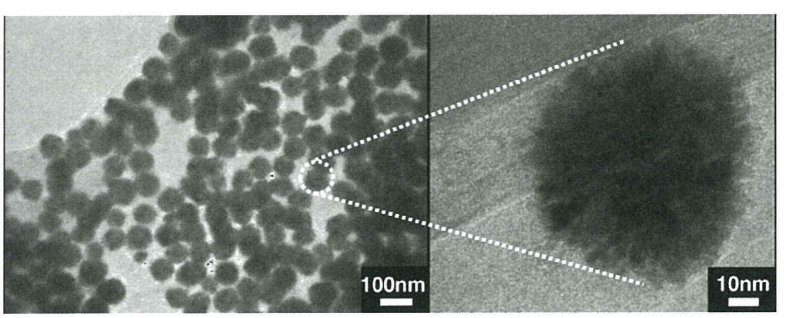

Fig. 5. TEM images of spherical moss-like Pd–DNA hybrid nanoparticles.

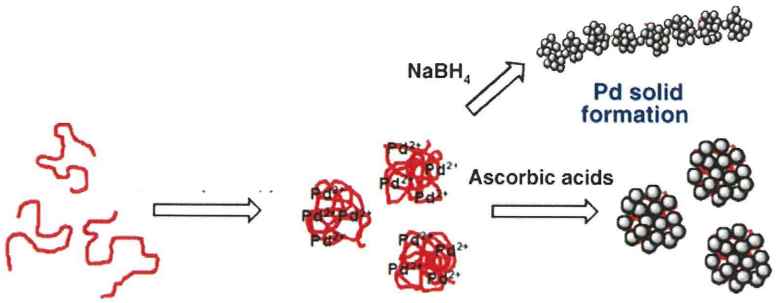

Fig. 7. Schematic illustration of the Pd–DNA hybrid nanostructure formation.

hydrogen sensors. Many sensors, which exhibit physical changes when exposed to hydrogen, have been fabricated and tested [28,29].

Palladium (Pd) is an attractive option as a hydrogen sensor in fuel cells. Pd reacts with hydrogen gas to form PdH_x [30]; this change increases the electrical resistance and volume of Pd materials. Selective adsorption of hydrogen can be detected from changes in mass [31,32], volume [33], optical constant [34,35], and/or electrical resistivity [36,37].

However, Pd-based hydrogen sensors have major obstacles. First, the response time for these devices is too slow to permit useful, real-time monitoring of flowing gas streams. Second, Pd is poisoned upon exposure to reactive species that chemisorb onto the Pd surface and block the adsorption sites necessary for hydrogen gas (H_2). To overcome the above problems, Favier et al. have reported a Pd mesowire-based sensor to detect H_2 based upon resistivity changes caused not by surface absorption, but by changes in the structure of the wire itself [38]. The resistance of this mesowire-based H_2 sensor decreases with the H_2 concentration, which is completely opposite to the behavior of the traditional resistance-based H_2 sensors. Hence, they proposed a new H_2 sensor and H_2 switch using break junctions in Pd mesowire arrays [40]. Below we demonstrate the performance and mechanism of operation for Pd–DNA hybrid nanostructure H_2 sensors.

To measure the hydrogen-sensing current of the resultant Pd–DNA hybrid nanostructures, two gold-film lines were deposited 1 mm apart on a glass plate using an ion-coating instrument. These lines were connected with a potentiostatic control instrument (1255B and SI1287, Solartron Analytical, Hampshire, UK). A paraffin frame (seating rim: 1×3 mm) was placed between the gold electrodes; then Pd–DNA nanostructures (0.02 mg) were added to the frame. The applied hybrid nanostructures were then dried under a vacuum. A 1 V voltage was applied to the sensor chip under sealed conditions. The gas in the sealed case was switched every 5 min between neat nitrogen gas and hydrogen-containing nitrogen gas.

Fig. 8 shows the current response of Pd–DNA hybrid nanostructures for a cyclic exchange of nitrogen and 1% hydrogen-containing nitrogen gases at atmospheric pressure and room temperature. Both samples show a clear response for the cyclic gas exchanges; the current increases in the presence of H_2, but decreases in the absence of H_2. This opposite response of the electrical resistivity compared to traditional resistance-based sensors seems to be due to the existence of nanoscopic break junctions between Pd primary nanoparticles in moss-like hybrid nanoparticles.

Electronic H_2 sensors based on a change in the resistivity can be easily miniaturized for use in fuel cells. Fig. 9 shows the mechanism for traditional resistance-based sensors and Pd–polyelectrolyte hybrid nanoparticle sensors. For traditional resistance-based sensors where Pd materials are connected (i.e., they lack break junctions) (Fig. 9(a)), the current response

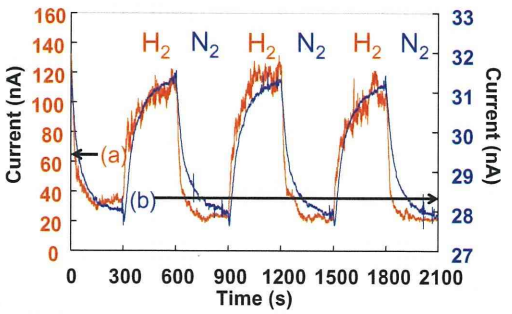

Fig. 8. Current responses of two types of Pd–DNA hybrid nanostructures for cyclic carrier-gas exchange: (a) nanoparticles synthesized by ascorbic acid reduction (red line); and (b) nanonecklaces synthesized by $NaBH_4$ reduction (blue line). Hydrogen concentration is 1%.

decreases when PdH_x is formed in the presence of H_2. In contrast, the current of a Pd mesowire-based resistive sensor with high-resistance break junctions increases because the increased volume of Pd materials in hydrogen-containing atmospheres closes the break junction at the Pd mesowire junction [38,40]. In our experiments, the behavior of the Pd–DNA hybrid nanostructures in an exchanged cyclic atmosphere shows a unique switch response that depends on the volume expansion (Fig. 9(b)).

To analyze nanostructural factors related to the volume-expansion response for H_2, we compared the current response of Pd–DNA hybrid nanostructures. Pd–DNA nanostructures synthesized by ascorbic acids reduction (Fig. 4) display a larger current change and a higher sensitivity for H_2 than those synthesized by $NaBH_4$ reduction (Fig. 6). This result might be due to the decrease in the empty nanospaces between Pd primary nanoparticles in the moss-like hybrid nanoparticles by fusion between primary nanoparticles. We estimated the sensitivity of the Pd–DNA nanostructures synthesized by ascorbic acid reduction (Fig. 8(a)) from the relative resistance. The ratio of the variation of resistance in a cyclic atmosphere exchange to the resistance in a hydrogen-free gas ($\Delta R/R_0$) exceeds 100% for a 1% hydrogen gas, which is several hundred times the value reported for a traditional resistance-based H_2 sensor [37,39].

The response time of Pd–DNA hybrid nanoparticles in a cyclic atmosphere exchange shows a high-conductivity state in the presence of H_2 and a low-conductivity state in the absence of H_2, i.e., an on–off current response time less than 1 min. The response of the Pd-based H_2 sensors depends on the diffusion process of hydrogen into the Pd lattice because the dissociative adsorption of hydrogen molecules on a Pd surface is fast. Therefore, the relatively fast on–off response of Pd–DNA in a low concentration of H_2 is due to Pd nanostructures constructed from Pd primary nanoparticles in the Pd–DNA hybrid nanoparticles. In addition, Pd–DNA nanostructures synthesized by ascorbic acid reduction have a

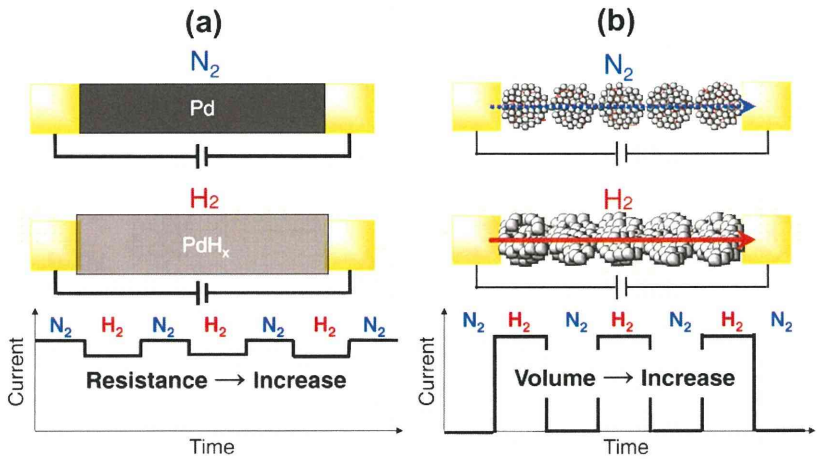

Fig. 9. Schematic illustration of the mechanism of electronic H_2 sensors for (a) traditional Pd materials and (b) Pd–DNA hybrid nanostructures. Data reproduced from Ohara et al. [4].

faster current change and response for H_2 than those synthesized by $NaBH_4$ reduction. Considering that the Pd primary nanoparticles in Pd–DNA hybrid nanonecklace structures synthesized by $NaBH_4$ reduction are fused due to excessive growth of primary nanoparticles, the size of Pd primary nanoparticles may influence the H_2 response.

To observe the detection limit of Pd–DNA hybrid nanostructures, we measured the current response in a low H_2 concentration. Consequently, Pd–DNA hybrid nanoparticles synthesized by ascorbic acid reduction show a volume-expansion response in an atmosphere of 0.05% hydrogen gas. However, a response is not observed in the presence of 0.01% hydrogen gas. The detection limit of Pd–DNA nanoparticles is lower than that of Pd mesowire arrays (1%), which shows a current response depending on volume expansion [38,40].

4. Pd–CNT hybrid nanostructures

To improve the detection limit of Pd-based H_2 sensors down to 0.01%, we recently fabricated Pd–CNT hybrid nanostructures. Fig. 10 depicts the experimental approach to arrange Pd nanoparticles on sodium dodecyl sulfate (SDS)-functionalized single-walled carbon nanotube (SWCNT). First, big bundles of SWCNT are separated into individual and/or small bundle tubes by forming supramolecular self-assemblies of SDS half-cylinders on the surface of SWCNT [41,42]. Then Pd(II) ions are selectively absorbed onto the surface of a SDS supramolecular self-assembly due to the electrostatic interaction between the Pd(II) cation and the anionic groups of sulfate in SDS molecules. Finally, Pd nanoparticles less than 5 nm are synthesized on the nanotubes by a photoreduction reaction and form helical nanostructures wrapped around a SWCNT template via the SDS supramolecular self-assembly.

The resultant nanostructures of the Pd nanoparticles on the surface of SDS-functionalized SWCNT have been characterized by high-resolution TEM. Pd nanoparticles form ordered nanostructures where Pd nanoparticles are arranged on the surface of SWCNT (Fig. 11). These nanostructures are very similar to those using copolymers as a soft template [43–48]. Because SDS, the soft template, forms a periodic supramolecular self-assembly on a SWCNT, the deposited Pd nanoparticles also form ordered periodic nanostructures on the surface of a SWCNT. Such periodic nanostructures are clearly observed by high-resolution TEM (Fig. 11(a)). The Pd nanoparticles are 2.5 ± 0.5 nm with an inter-nanoparticle distance of 4.5 ± 0.5 nm along the orientation parallel to the tube axis. This value is the same as the lateral striations of SDS half-cylinders. This observation indicates that Pd nanoparticles are selectively deposited onto a SDS-functionalized SWCNT along the half-cylinders of the SDS supramolecular self-assemblies wrapped around a SWCNT. The ordered nanostructures of Pd nanoparticles have been observed in detail (Fig. 11(b and d). Fig. 11(b) shows a clear image of Pd nanoparticles forming ordered nanostructures wrapping around the SWCNT. The nanostructures have a right helix twist with a tilt angle of −6° relative to the tube axis. The tilt angle of the Pd nanostructures depends on the SDS half-cylinders, which act as a soft template. In our experiment, ordered nanostructures of Pd nanoparticles with various helices or tilt angles are also observed (Fig. 11(c)). Interestingly, Fig. 11(d) shows the periodic nanostructures of Pd nanoparticles with various helices and tilt angles on an individual bundle of SWCNT. These observations indicate various helices of half-cylinders in the SDS supramolecular self-assembly can wrap around

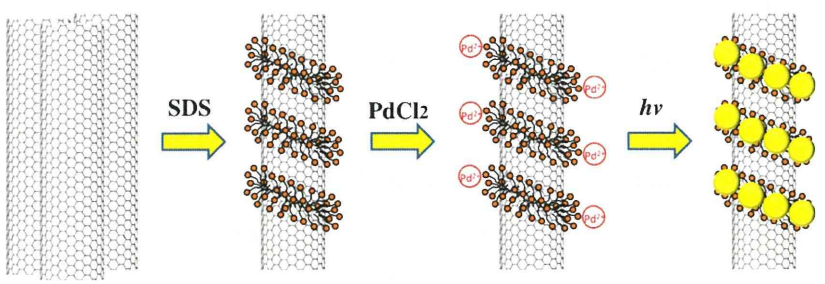

Fig. 10. A schematic approach for the site-selective synthesis of ordered nanostructures of Pd nanoparticles wrapped on SWCNTs. Data reproduced from Tan et al. [5].

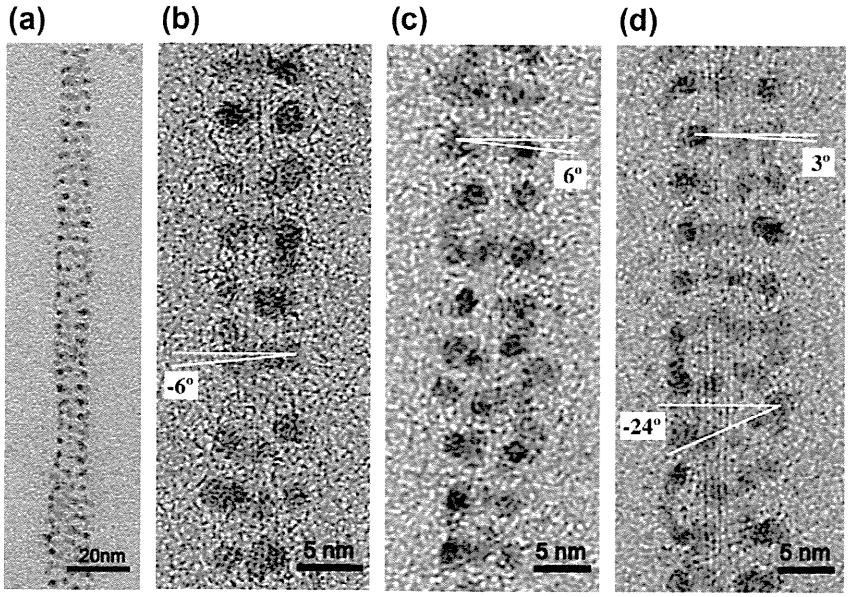

Fig. 11. TEM images of Pd nanoparticles selectively deposited on the SDS-functionalized SWCNTs, (a) Pd nanoparticles form a unique helical nanostructure wrapped around a nanotube. (b) Pd nanoparticles wrap in a right helix with a tilt angle of −6° relative to the nanotube axis. (c) Pd nanoparticles wrap in a left helix around a SWCNT with a tilt angle of 6° relative to the tube axis. (d) Pd nanoparticles organize as a left helix wrapped around the tube with a tilt angle of 3° and a right helix with a tilt angle of −24° relative to the nanotube axis.

an individual bundle of SWCNT. Hence, we believe that reliable, ultra-compact and safe hydrogen sensor devices for use in fuel cells will be fabricated using the Pd–CNT hybrid nanostructures.

5. Conclusions

We have compacted λ-DNA using Pd(II) ions, and described the formation of unique moss-like Pd–DNA hybrid nanostructures by a combination of metallization and DNA compaction. By reducing Pd under conditions where DNA is compacted, Pd nanoparticles are formed on DNA so that the primary nanoparticles assemble in a moss-like manner on the compacted DNA conformation. Employing ascorbic acid as a reducing reagent promotes the morphological homogeneity of the assembled Pd–DNA hybrid nanoparticles. Additionally, we demonstrate that Pd–DNA hybrid nanoparticles are highly sensitive hydrogen sensors, which possess a switch response that depends on the volume expansion of the metallic nanostructures in a cyclic atmosphere exchange. Furthermore, we report a facile route to selectively deposit and arrange Pd nanoparticles on a CNT via a supramolecular self-assembly of SDS as a soft template. We believe that high-performance H_2 sensors, catalytic activity, electrodes for polymer electrolyte fuel cells, and (bio)chemical sensors will be fabricated using these Pd-based hybrid nanostructures.

Acknowledgments

This work was supported by Industrial Technology Research Grant Program in '05 from New Energy and Industrial Technology Development Organization (NEDO) of Japan. This research was also partly supported by a Scientific Research Grant and Grant-in-Aid for Cooperative Research Project of Advanced Materials Development and Integration of Novel Structured Metallic and Inorganic Materials from the Ministry of Education, Culture, Sports, Science and Technology of Japan.

References

[1] S. Ohara, T. Adschiri, Nanostructure and function (characterization of local nanostructure), in: M. Hosakawa, K. Nogi, M. Naito, T. Yokoyama (Eds.), Nanoparticle Technology Handbook, Elsevier, The Netherlands, 2007, pp. 269–270.
[2] I.L. Medintz, H.T. Uyeda, E.R. Goldman, H. Mattoussi, Quantum dot bioconjugates for imaging, labelling and sensing, Nature Mater. 4 (2005) 435–446.
[3] Y. Hatakeyama, M. Umetsu, S. Ohara, F. Kawadai, S. Takami, T. Naka, T. Adschiri, Homogenous spherical moss-like assembly of Pd nanoparticles by using DNA compaction – Application of DNA-Pd hybrid materials to volume-expansion hydrogen switches, Adv. Mater. 20 (2008) 1122–1128.
[4] S. Ohara, Y. Hatakeyama, M. Umetsu, K. Sato, T. Naka, T. Adschiri, Palladium-polyelectrolyte hybrid nanoparticles for hydrogen sensor in fuel cells, J. Power Sour. 193 (2009) 367–370.
[5] Z. Tan, H. Abe, M. Naito, S. Ohara, Arrangement of palladium nanoparticles templated by supramolecular self-assembly of SDS wrapped on single-walled carbon nanotubes, Chem. Comm. 46 (2010) 4363–4365.
[6] C.A. Mirkin, R.L. Letsinger, R.C. Mucic, J.J. Storhoff, A DNA-based method for rationally assembling nanoparticles into macroscopic materials, Nature 382 (1996) 607–609.
[7] K. Sato, K. Hosokawa, M. Maeda, Rapid aggregation of gold nanoparticles induced by non-cross-linking DNA hybridization, J. Am. Chem. Soc. 125 (2003) 8102–8103.
[8] C. Mao, W. Sun, N.C. Seeman, Designed two-dimensional DNA holliday junction arrays visualized by atomic force microscopy, J. Am. Chem. Soc. 121 (1999) 5437–5443.
[9] S. Xiao, F. Liu, A.E. Rosen, J.F. Hainfeld, N.C. Seeman, K. Musier-Forsyth, R.A. Kiehl, Selfassembly of metallic nanoparticle arrays by DNA scaffolding, J. Nanoparticle Res. 4 (2002) 313–317.
[10] Y.Y. Pinto, J.D. Le, N.C. Seeman, K. Musier-Forsyth, T.A. Taton, R.A. Kiehl, Sequence-encoded self-assembly of multiple-nanocomponent arrays by 2D DNA scaffolding, Nano. Lett. 5 (2005) 2399–2402.
[11] J.K.N. Mbindyo, B.D. Reiss, B.R. Martin, C.D. Keating, M.J. Natan, T.E. Mallouk, DNA-directed assembly of gold nanowires on complementary surfaces, Adv. Mater. 13 (2001) 249–254.
[12] K. Keren, M. Krueger, R. Gilad, G. Ben-Yoseph, U. Sivan, E. Braun, Sequence-specific molecular lithography on single DNA molecules, Science 297 (2002) 72–75.
[13] E. Braun, Y. Eichen, U. Sivan, G. Ben-Yoseph, DNA-templated assembly, electrode attachment of a conducting silver wire, Nature 391 (1998) 775–778.
[14] A.A. Zinchenko, K. Yoshikawa, D. Baigl, DNA-templated silver nanorings, Adv. Mater. 17 (2005) 2820–2823.
[15] J. Richter, R. Seidel, R. Kirsch, M. Mertig, W. Pompe, J. Plaschke, H.K. Schackert, Nanoscale palladium metallization of DNA, Adv. Mater. 12 (2000) 507–510.
[16] J. Richter, M. Mertig, W. Pompe, Construction of highly conductive nanowires on a DNA template, Appl. Phys. Lett. 78 (2001) 536–538.

[17] R. Seidel, L.C. Ciacchi, M. Weigel, W. Pompe, M. Mertig, Synthesis of platinum cluster chains on DNA templates: Conditions for a template-controlled cluster growth, J. Phys. Chem. B 108 (2004) 10801–10811.
[18] C.F. Monson, A.T. Woolley, DNA-templated construction of copper nanowires, Nano. Lett. 3 (2003) 359–363.
[19] G.B. Onoa, G. Cervantes, V. Moreno, M.J. Prieto, Study of the interaction of DNA with cisplatin and other Pd(II) and Pt(II) complexes by atomic force microscopy, Nucleic Acids Res. 26 (1998) 1473–1480.
[20] Y. Yoshikawa, K. Yoshikawa, Diaminoalkanes with an odd number of carbon-atoms induce compaction of a single double-stranded DNA chain, FEBS Lett. 361 (1995) 277–281.
[21] A.A. Zinchenko, V.G. Sergeyev, K. Yamabe, S. Murata, K. Yoshikawa, DNA compaction by divalent cations: Structural specificity revealed by the potentiality of designed quaternary diammonium salts, Chem. Bio. Chem. 5 (2004) 360–368.
[22] R.W. Wilson, V.A. Bloomfield, Counterion-induced condensation of deoxyribonucleic-acid, Light-scattering study Biochem. 18 (1979) 2192–2196.
[23] G.S. Manning, Packaged DNA, An elastic model, Cell Biophys. 7 (1985) 57–89.
[24] J. Duguid, V.A. Bloomfield, J. Benevides, G.J. Thomas Jr., Raman spectroscopy of DNA-metal complexes. I. Interactions and conformational effects of the divalent cations: Mg, Ca, Sr, Ba, Mn, Co, Ni, Cu, Pd, and Cd, Biophys, Biophys. J. 65 (1993) 1916–1928.
[25] D.P. Bancroft, C.A. Lepre, S.J. Lippard, 195 Pt NMR kinetic and mechanistic studies of cis- and trans-diamminedichloroplatinum(II) binding to DNA, J. Am. Chem. Soc. 112 (1990) 6860–6871.
[26] J. Richter, Metallization of DNA, Physica E: Low-Dimensional Systems Nanostructure 16 (2003) 157–173.
[27] Y. Yoshikawa, M. Suzuki, N. Chen, A.A. Zinchenko, S. Murata, T. Kanbe, T. Nakai, H. Oana, K. Yoshikawa, Ascorbic acid induces a marked conformational change in long duplex DNA, Eur. J. Biochem. 270 (2003) 3101–3106.
[28] W. Shin, M. Nishibori, Y. Choi, K. Tajima, N. Izu, I. Matsubara, N. Murayama, Integration of ceramic catalyst on micro-thermoelectric gas sensor, Sens. Actuators B 118 (2006) 283–291.
[29] K. Yamanaka, S. Ishikawa, N. Nakaso, N. Takeda, D.Y. Sim, T.Y. Mihara, A. Mizukami, I. Satoh, S. Akao, Y. Tsukahara, Ultramultiple roundtrips of surface acoustic wave on sphere realizing innovation of gas sensors, IEEE Trans. 53 (2006) 793–801.
[30] C. Christofides, A. Mandelis, Solid-state sensors for trace hydrogen gas-detection, J. Appl. Phys. 68 (1990) R1–R30.
[31] R.V. Bucur, V. Mecca, T.B. Flanagan, The kinetics of hydrogen (deuterium) sorption by thin palladium layers studied with a piezoelectric quartz crystal microbalance, Surf. Sci. 54 (1976) 477–488.
[32] G.A. Frazier, R. Glosser, Phase diagrams of thin films of the palladium hydrogen system using a quartz crystal thickness monitor, J. Phys. D: Appl. Phys. 12 (1979) L113–L115.
[33] P.J. Shaver, Bimetal Strip Hydrogen Gas Detectors, Rev. Sci. Instrum. 40 (1969) 901–905.
[34] A. Mandelis, J.A. Garcia, Pd/PVDF thin film hydrogen sensor based on laser-amplitude-modulated optical-transmittance. dependence on H-2 concentration and device physics, Sens. Actuator B 49 (1998) 258–267.
[35] Y. Okuhara, M. Takata, Recovery characteristics of optical hydrogen sensor using Pd thin film: Behaviour of three-stage hydrogen desorption, Bull. Mater. Sci. 22 (1999) 85–87.
[36] R.C. Hughes, W.K. Schubert, Thin films of Pd/Ni alloys for detection of high hydrogen concentrations, J. Appl. Phys. 71 (1992) 542–544.
[37] S.F. Yu, U. Welp, L.Z. Hua, A. Rydh, K.W. Kwok, H.H. Wang, Fabrication of palladium nanotubes and their application in hydrogen sensing, Chem. Mater. 17 (2005) 3445–3450.
[38] F. Favier, E.C. Walter, M.P. Zach, T. Benter, R.M. Penner, Hydrogen sensors and switches from electrodeposited palladium mesowire arrays, Science 293 (2001) 2227–2231.
[39] E.C. Walter, R.M. Penner, H. Liu, K.H. Ng, M.P. Zach, F. Favier, Sensors from electrodeposited metal nanowires, Sur. Interface Anal. 34 (2002) 409–412.
[40] E.C. Walter, F. Favier, R.M. Penner, Palladium mesowire arrays for fast hydrogen sensors and hydrogen-actuated switches, Anal. Chem. 74 (2002) 1546–1553.
[41] H. Xu, H. Abe, M. Naito, H. Ichikawa, Y. Fukumori, S. Endoh, Immobilization of highly-dispersed single-walled carbon nanotubes in biocompatible and water-soluble solid matrix, J. Ceram. Soc. Jpn. 116 (2008) 965–967.
[42] Z. Tan, H. Xu, H. Abe, M. Naito, S. Ohara, Anisotropic polyhedral self-assembly of Ag-CNT nanocomposites, J. Nanosci. Nanotechnol. 10 (2010) 3978–3982.
[43] M. Zheng, A. Jagota, E.D. Semke, B.A. Diner, R.S. McLean, S.R. Lustig, R.E. Richardson, N.G. Tassi, DNA-assisted dispersion and separation of carbon nanotubes, Nat. Mater. 2 (2003) 338–342.
[44] A. Nish, J.-Y. Hwang, J. Doig, R.J. Nicholas, Highly selective dispersion of singlewalled carbon nanotubes using aromatic polymers, Nat. Nanotechnol. 2 (2007) 640–646.
[45] C. Thauvin, S. Rickling, P. Schultz, H. Celia, S. Meunier, C. Mioskowski, Carbon nanotubes as templates for polymerized lipid assemblies, Nat. Nanotechnol. 3 (2008) 743–748.
[46] S.-Y. Ju, J. Doll, I. Sharma, F. Papadimitrakopoulos, Selection of carbon nanotubes with specific chiralities using helical assemblies of flavin mononucleotide, Nat. Nanotechnol. 3 (2008) 356–362.
[47] S.-Y. Ju, W.P. Kopcha, F. Papadimitrakopoulos, Brightly fluorescent single-walled carbon nanotubes via an oxygen-excluding surfactant organization, Science 323 (2009) 1319–1323.
[48] X. Tu, S. Manohar, A. Jagota, M. Zheng, DNA sequence motifs for structure-specific recognition and separation of carbon nanotubes, Nature 460 (2009) 250–253.

View Online / Journal Homepage / Table of Contents for this issue
Dynamic Article Links

Journal of Materials Chemistry

Cite this: J. Mater. Chem., 2012, 22, 9041

www.rsc.org/materials

PAPER

Continuous hydrothermal synthesis of 3,4-dihydroxyhydrocinnamic acid-modified magnetite nanoparticles with stealth-functionality against immunological response†

Takanari Togashi,*[a] Seiichi Takami,[b] Kazuyoshi Kawakami,[c] Hideki Yamamoto,[c] Takashi Naka,[d] Koichi Sato,[d] Keietsu Abe[e] and Tadafumi Adschiri[a]

Received 17th January 2012, Accepted 15th February 2012
DOI: 10.1039/c2jm30325f

In our study, water dispersible magnetite (Fe_3O_4) nanoparticles were continuously synthesized in water under high temperature and pressure in the presence of 3,4-dihydroxyhydrocinnamic acid (DHCA) by using a tubular flow reactor. The prepared Fe_3O_4 nanoparticles were well dispersed in water because the surfaces of the nanoparticles were fully covered by DHCA molecules and the –COOH groups in the DHCA molecules were exposed to the surrounding water. Cytokines such as IL-12 and TNF-α were not produced from the dendritic cells of mice by co-incubation with our synthesized Fe_3O_4. This indicates that the synthesized Fe_3O_4 had no immune stimulating property for the dendritic cells of the mouse. Therefore, our synthesized Fe_3O_4 nanoparticles are suitable for biological applications such as magnetic resonance imaging contrast agents and carriers for drug and gene delivery, and in areas such as hyperthermia therapy for cancer, biosensors, and tissue engineering.

Introduction

Magnetic nanoparticles have attracted increasing interest among researchers for their potential applications across a wide range of fields.[1–4] Magnetite (Fe_3O_4) is a representative of such nanoparticles. Recently, several biological applications of Fe_3O_4 have been proposed and studied; these include its uses as a carrier for drug and gene delivery, in hyperthermia therapy for cancer, in biosensors, and in tissue engineering.[5–8]

Various methods of preparing Fe_3O_4 nanoparticles have been studied.[9–13] Among these methods, the thermal decomposition of an iron salt in the presence of long-alkyl-chain surfactants yields Fe_3O_4 nanoparticles with high crystallinity, narrow particle-size distribution, and superparamagnetic properties.[9,11–13] However, the prepared Fe_3O_4 nanoparticles were dispersed in nonpolar solvents and not in water, because the surfaces of the prepared Fe_3O_4 nanoparticles were covered with long-alkyl-chains. In addition, Fe_3O_4 nanoparticles are hydrophobic in nature.

For the abovementioned medical applications, Fe_3O_4 nanoparticles should be sufficiently small and well dispersible in water and blood without leading to their aggregation. In addition, they should not be captured by phagocytes including macrophages, *i.e.*, the particles should be stealthy against the immunological responses of the human body.[14] In order for iron oxides to possess long half-lives in the bloodstream, they can be coated with molecules such as citrates[15] and hydrophilic polymers.[16–19] Recently, a variety of ligand-exchange strategies for inorganic nanoparticles that enable hydrophobic surface modification have been developed.[20–27] However, in these methods, besides the practical difficulties of phase transfer, the stability of the particle dispersions is an additional major concern.[28] Therefore, the requirement is to achieve a one-step synthesis of water-dispersible Fe_3O_4 nanoparticles (preferably with the use of nontoxic chemicals) that do not stimulate immunological response.

In this study, water-dispersible, stealth-functional Fe_3O_4 nanoparticles were synthesized using a flow-type reactor. In order to disperse the Fe_3O_4 nanoparticles in water, the Fe_3O_4 surface must be modified with a hydrophilic functional group; for this purpose, we used 3,4-dihydroxyhydrocinnamic acid (DHCA, Scheme 1); DHCA is regarded as a biofriendly molecule because it is extracted from certain fruits and vegetables.[29] The synthesized Fe_3O_4 nanoparticles disperse well in water because the –COOH group from the DHCA is present on the Fe_3O_4 surface. In addition, the synthesized Fe_3O_4 has no immune-stimulating properties for dendritic cells; this absence of immune

[a]*Advanced Institute for Material Research(WPI-AIMR), Tohoku University 2-1-1, Katahira, Aoba-ku, Sendai 980-8577, Japan. E-mail: togashi@tagen.tohoku.ac.jp; Fax: +81-22-217-6323; Tel: +81-22-217-6323*
[b]*Institute for Multidisciplinary for Advanced Material, Tohoku University, 2-1-1 Katahira, Aoba-ku, Sendai, Miyagi 980-8577, Japan*
[c]*Department of Medical Microbiology and Immunology, Tohoku University, 2-1 Seiryo-cho, Aoba-ku, Sendai, Miyagi 985-8575, Japan*
[d]*Innovative Materials Engineering Laboratory, National Institute for Material Science, Sengen 1-2-1, Tsukuba, Ibaraki 305-0047, Japan*
[e]*New Industry Creation Hatchery Centre, Tohoku University, 6-6-10 Aoba, Aoba-ku, Sendai, Miyagi 980-8579, Japan*
† Electronic supplementary information (ESI) available. See DOI: 10.1039/c2jm30325f

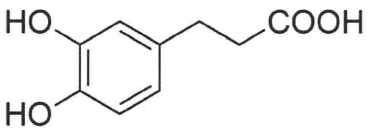

Scheme 1 Chemical structure of DHCA.

stimulation is necessary for the nanoparticles to have a sufficient half-life in blood.

Materials and methods

Chemicals

Iron sulfate hexahydrate ($FeSO_4 \cdot 6H_2O$, 99%) and potassium hydroxide (KOH, 99%) were purchased from Kojundo Chemical Laboratory Co. Ltd. 3,4-Dihydroxyhydrocinnamic acid (DHCA, 98%) was purchased from Aldrich. These chemicals were used in our experiment without further purification.

Synthesis

The reactant solution was prepared by mixing equal volumes of $FeSO_4$ (40 mM) and DHCA (40 mM) aqueous solutions. The pH of the solution was adjusted to 9.5 by adding 5.0 M KOH aqueous solution. Magnetite nanoparticles were synthesized using a lab-scale plug flow reactor (Scheme 2). Deionized water was pumped using a high-pressure pump (Nihon Seimitsu Kagaku, NP-KX-540) at a rate of 10 ml min^{-1} through a stainless steel (SUS 316) tube with an inner diameter of 1.8 mm. The tube was heated using an electronic furnace. The reaction mixture was separately pumped through another tube at a rate of 3 ml min^{-1}. The reactants and the heated water were mixed at a junction to raise the temperature of the reaction mixture instantaneously. The temperature of the mixed flow was monitored by a thermocouple and controlled by changing the temperature of the furnace. The temperatures of the heated water and the mixed flow were set to ~450 and ~360 °C, respectively. After the mixture from the furnace was passed through the isothermal zone, the product was quickly cooled to room temperature with a water jacket. The typical residence time for the product was 1.8 s. The cooled product was filtered through a 0.5 μm filter (Swegelok, TF Series) to remove accidentally produced aggregates. Subsequently, the product was released from a back-pressure regulator (TESCOM, 26-1700 Series) that maintained the system pressure at 30 MPa.

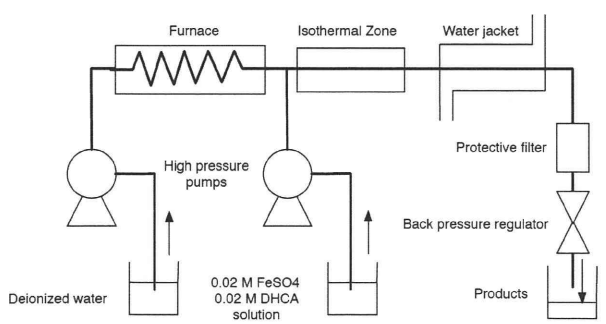

Scheme 2 Schematic of experimental apparatus.

The products were washed into 0.01 M KOH aqueous solution using 3 cycles of centrifugation, decantation, and redispersion. The collected products dispersed well in distilled water and the aqueous solution appeared black.

Characterization of magnetite nanoparticles

Powder X-ray diffraction (XRD) patterns of the dried samples were recorded on a RIGAKU Ultima IV instrument (RIGAKU, Japan) with the angle 2θ ranging from 20° to 80°. Transmission electron microscope (TEM) images were obtained using a Hitachi H7650 at 100 kV. All samples were prepared by evaporating diluted suspensions on a carbon-coated copper grid.

Fourier transform infrared spectroscopy (FTIR) measurements were performed using an FT/IR 680 spectrometer (Jasco Co. Ltd., Japan). The spectra were recorded in the wavenumber range of 4000–600 cm^{-1}. The samples were ground and mixed with KBr and subsequently pressed to form pellets. The background spectrum was taken using a pure KBr pellet as the standard reference.

Zeta-potential measurements of the obtained colloidal system were performed using a Zetasizer Nano instrument (Malvern instruments) in capillary zeta-potential cells. pH titrations were performed using 0.01 M HCl and 0.01 M NaOH solutions in an auto-titration unit.

Preparation and culture of dendritic cells

Bone marrow (BM) cells from C57BL/6 mice were cultured at a density of 2×10^5 ml^{-1} in 10 ml RPMI1640 medium supplemented with 10% FCS, 100 U ml^{-1} penicillin G, 100 μg ml^{-1} streptomycin, and 50 μM 2-mercaptoethanol containing 20 ng ml^{-1} murine granulocyte-macrophage colony-stimulating factor (Wako, Osaka, Japan). On day 3, another 10 ml of the same medium was added; on day 6, a half-change was performed using the GM–CSF-containing culture medium. On day 8, non-adherent cells were collected and used as BM-derived dendritic cells. The obtained cells were cultured at a density of 1×10^5 ml^{-1} with 0.01–0.1 mg ml^{-1} of Fe_3O_4 for 24 h at 37 °C in a 5% CO_2 incubator. Experiments using mice were conducted according to the guidelines approved by the ethics committee of Tohoku University.

Result and discussion

Characterization of magnetite nanoparticles

In order to identify the crystal structure and evaluate the crystallite size, the products were analyzed by powder XRD (Fig. 1). All powder XRD patterns are identified as those of magnetite (Fe_3O_4 JCPDS 86-1354); the lattice constants are a = 8.42, 8.42, 8.43, and 8.43 Å for reaction temperatures of 230, 260, 300, and 350 °C, respectively; these values are in good agreement with the reported value of a = 8.432 Å.[30] Crystallite size was evaluated using Scherrer's equations with a peak of the {311} plane. The Fe_3O_4 crystallite sizes were 10.5, 13.2, 16.2, and 17.6 nm for reaction temperatures of 230, 260, 300, and 350 °C, respectively, thereby suggesting that crystallite size increases with reaction temperature.

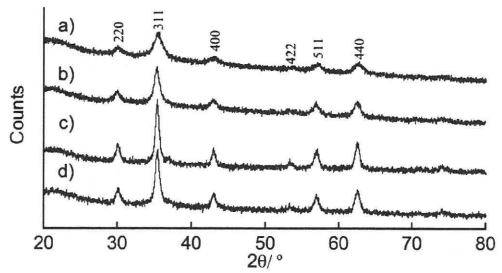

Fig. 1 Powder X-ray diffraction (XRD) pattern of Fe_3O_4 nanoparticles synthesized at various temperatures: (a) 230 °C, (b) 260 °C, (c) 300 °C, and (d) 350 °C.

In order to observe the morphology and size of the synthesized Fe_3O_4 particles, we examined the products using TEM (Fig. 2). The TEM images show that the particle morphology was spherical for all reaction temperatures. The average particle sizes were 10.2, 13.3, 16.3, and 18.0 nm for reaction temperatures of 230, 260, 300, and 350 °C, respectively. These sizes were almost identical to the obtained crystalline sizes evaluated by powder XRD, thereby indicating that the synthesized particles were single crystals.

The synthesized Fe_3O_4 nanoparticles dispersed well in water (Fig. S1†). The DHCA molecules in the reaction solution conjugated with the surface of nanoparticles because the catechol group has high affinity with metal oxides through coordination bonding.[31,32] The conjugated DHCA molecules displayed –COOH groups toward the surrounding water and therefore the synthesized Fe_3O_4 become dispersible in water. In order to confirm this hypothesis, we measured the FTIR spectrum of the magnetite nanoparticles synthesized at 300 °C (Fig. 3(a)). The sharp peaks at 1484 and 1259 cm^{-1} are characteristic of the catechol anion that binds covalently to the metal oxide surface.[33,34] The sharp peak at 1627 cm^{-1} is assigned to the free –COOH group.[35] When the –COOH group binds with the Fe ion, a single peak at 1584 cm^{-1} should ideally appear in the FTIR spectrum.[36] However, in our study, this peak was not observed, thereby indicating that none of the –COOH groups of DHCA that conjugated to the synthesized Fe_3O_4 particles bound to Fe ions and aligned facing towards the solvent (Fig. 3(b)). This is why the synthesized Fe_3O_4 nanoparticles dispersed well in water.

In order to confirm the surface charge of the Fe_3O_4 nanoparticles, we measured their zeta potential with a zeta-potential analyzer. The isoelectric point of Fe_3O_4 is 4.0. The zeta potential of the Fe_3O_4 nanoparticles decreased gradually with decreasing pH and approached zero at a pH value of approximately 4.0 (Fig. 4). The isoelectric point of unmodified Fe_3O_4 is 8.00.[37] The pK_a of the DHCA –COOH group is 4.2;[38] this value is nearly identical to the isoelectric point of our synthesized Fe_3O_4 nanoparticles, thereby indicating the presence of the –COOH group on the surface of the nanoparticles. In addition, no precipitates were confirmed in synthesized Fe_3O_4 nanoparticle suspension within six months, thereby suggesting that the surface charge and solubility of the synthesized Fe_3O_4 nanoparticles are controlled by the –COOH groups.

We performed thermogravimetric measurements to evaluate the degree to which the DHCA molecules attach themselves to the surface of Fe_3O_4 nanoparticles (Fig. S2†). A significant

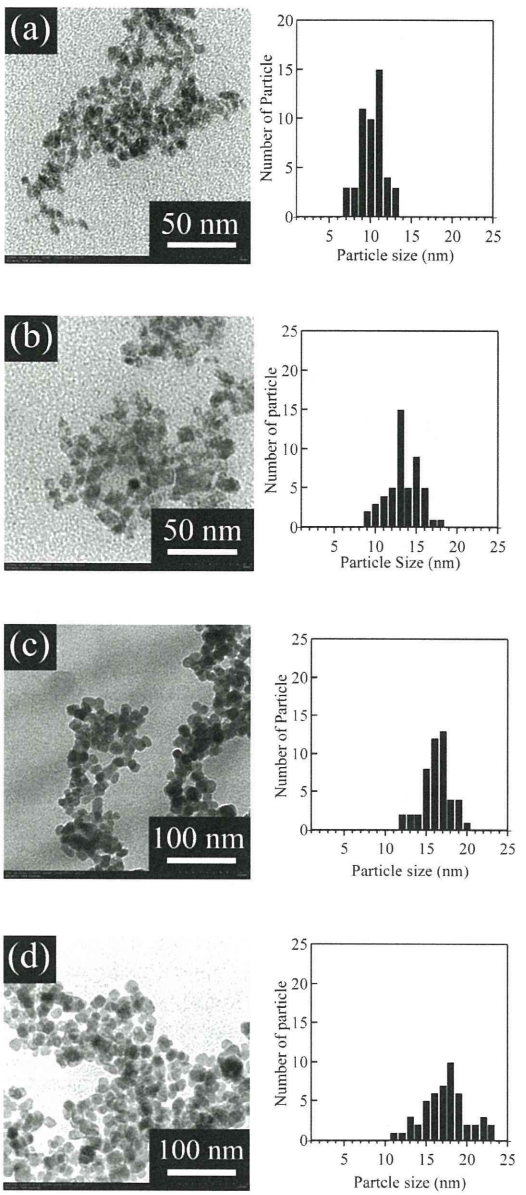

Fig. 2 TEM image and size distribution of Fe_3O_4 nanoparticles synthesized at (a) 230 °C, (b) 260 °C, (c) 300 °C, and (d) 350 °C.

decrease in weight is observed at 280 °C; this is attributed to DHCA desorption and decomposition according to a previous report.[39] The degree of DHCA coverage on all synthesized Fe_3O_4 nanoparticles is approximately 4 molecules nm^{-2}. This value does not change significantly with changing reaction temperature (Table S1†).

Magnetic properties of synthesized Fe_3O_4

We measured the magnetic properties of the synthesized water-soluble Fe_3O_4 nanoparticles using a superconducting quantum interference device (SQUID). Fig. 5 shows the magnetization-field (M–H) curve for the nanoparticles with a diameter of 16.2 nm, measured at 290 and 5 K. At 290 K, the nanoparticles have superparamagnetic properties; this is because the coercivity

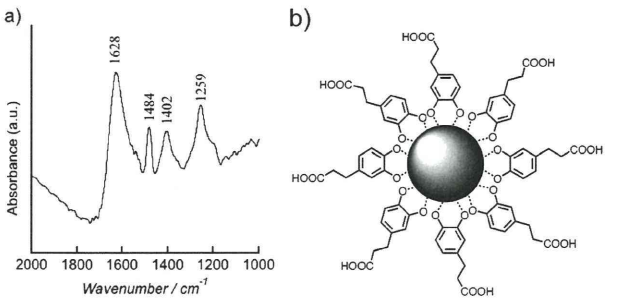

Fig. 3 (a) Typical FTIR spectrum and (b) predicted structure of Fe_3O_4 nanoparticles synthesized at 300 °C.

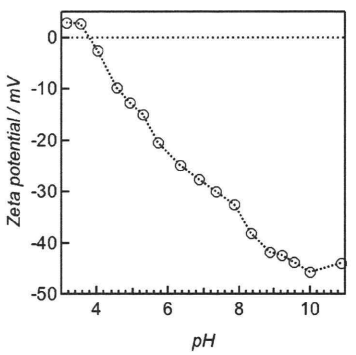

Fig. 4 Zeta potential of the Fe_3O_4 synthesized at 300 °C as a function of pH.

of the synthesized 16.2 nm diameter Fe_3O_4 nanoparticles is <10 Oe (Fig. 5(b)). In contrast, at 5 K, a typical ferromagnetic hysteresis loop with a remanence of 24.2 emu g^{-1} and a coercivity of 340 Oe can be observed because the thermal energy is insufficient to induce moment randomization. The saturation magnetic moments at 290 and 5 K are 75.43 and 86.67 emu g^{-1}, respectively (Fig. 5(a)).

In general, the saturation magnetic moment decreases when the size of a magnetite particle reduces to the order of nanometres. Several studies suggest that the lower magnetic saturation values for smaller Fe_3O_4 nanoparticles are caused either by an increasing spin-disorder effect at the particle surface, by the existence of canted spins if the particle is sufficiently small,[2,40] or by the surface magnetic moment of the coating

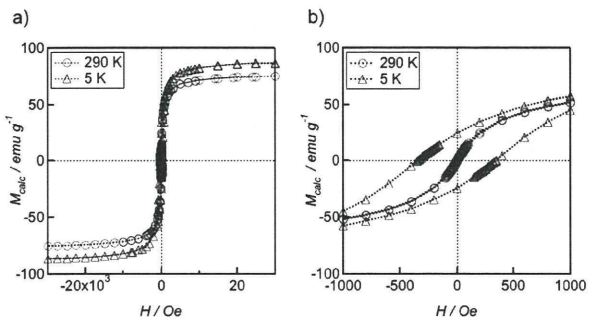

Fig. 5 (a) Whole and (b) magnified plots of magnetic properties of Fe_3O_4 nanoparticles synthesized at 300 °C, measured at 290 K (○) and 5 K (△).

agent.[41,42] However, in our case, the saturation magnetic moment of the synthesized magnetite nanoparticles is almost identical to the values reported for bulk magnetite (90 emu g^{-1} theoretical and 82 emu g^{-1} experimental).[43] The particle size (<10 nm) is not sufficiently small to magnetically observe the existence of a disordered spin-glass-like surface-layer effect and canted spins.[26] However, in our case, the depression of saturation magnetization was not observed. Therefore, the synthesized magnetite should act as an ideal magnetite and exhibit no negative size effect.

Immunological response for mouse dendritic cells

Macrophages are a critical element of the body's system of defense against disease. The introduction of nanoparticles into the body may affect the macrophages' defensive functions[44] by promoting macrophage activation as well as their phagocytic-, cytoskeletal-, and cytokine-releasing functions. If the macrophages are stimulated by the introduction of nanoparticles, there is uptake of nanoparticles by phagocytes and they cannot travel freely through blood vessels, thereby shortening the half-life of the nanoparticles in blood. Therefore, the suppression of nanoparticle stimulation of macrophages is required for biological applications of nanoparticles, particularly for *in vivo* situations.

In order to evaluate the degree of stimulation of immunological response, we measured the production of cytokine, IL-12, and TNF-α after co-incubating bone marrow dendritic cells (BM-DCs) of mice with our Fe_3O_4 nanoparticles (diameter 17.2 nm). Along with macrophages, BM-DCs are known to play an important role in the generation of an adequate immunological response in the presence of invasive material.[45] Fig. 6 shows the result of immunostimulation of BM-DCs, evaluated on the basis of the synthesized cytokine concentration. Cytokine was not produced from BM-DCs by co-incubation of Fe_3O_4 in the concentration range 1–100 μg ml^{-1}, whereas lipopolysaccharide (LPS) induced a striking response. This indicates that the synthesized DHCA-modified Fe_3O_4 nanoparticles do not stimulate immunological response. It has been reported that small nanoparticles (diameter 1–30 nm) can escape from phagocytes and travel through blood vessels with a reasonably high (>1 h) half-life.[44,46] In our study, the hydrodynamic

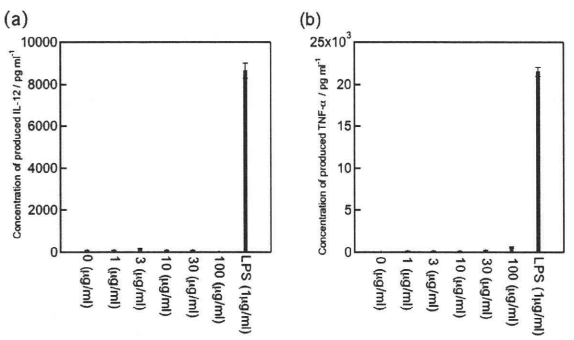

Fig. 6 Concentration of produced cytokines, (a) IL-12 and (b) TNF-α, as a measure of stimulated immunological response of BM-CDs toward various concentrations of DHCA-modified Fe_3O_4 nanoparticles with a diameter of 16.3 nm (0–100 μg ml^{-1}) and 1 μg of lipopolysaccharide (LPS).

diameter of the synthesized Fe_3O_4 nanoparticles was <20 nm, thereby indicating that the nanoparticles were highly dispersible in water media without coating by hydrophilic polymers such as polyethylene glycol. In addition, negatively charged particles are less likely to induce immunological response than positively charged particles.[47] Moreover, the synthesized Fe_3O_4 particle surfaces are negatively charged under neutral conditions; therefore, the immunological responses were suppressed by this surface charge effect. The abovementioned reasons are probably why the BM-DCs were not stimulated by the synthesized Fe_3O_4 nanoparticles. Therefore, we believe that our synthesized Fe_3O_4 nanoparticles have a long half-life in blood and travel stably through blood vessels.

Conclusion

DHCA-modified Fe_3O_4 nanoparticles were prepared using a continuous flow-type reactor. The synthesized Fe_3O_4 nanoparticle size was controlled by the reaction temperature. The nanoparticles dispersed well in water because their surface was covered with biofriendly DHCA molecules. Further, the –COOH group in the DHCA was exposed to the surrounding water, thereby contributing to good nanoparticle dispersion in water. The saturation magnetic moment of the synthesized Fe_3O_4 nanoparticles was nearly identical to that of bulk Fe_3O_4. The synthesized nanoparticles had superparamagnetic properties at room temperature and did not stimulate the dendritic cells of a test mouse. These results indicate that DHCA is one of the new suitable modifiers for preparing the water dispersible nanomaterials that can be applied for biomedical applications.

Acknowledgements

We thank Dr. Toru Takahashi, Dr. Akira Yoshimi, and Mr. Masahiro Noguchi for supporting this study. This work was supported by a Grant-in-Aid for Scientific Research (S) no. 20226015, a Grant-in-Aid for Scientific Research (A) no. 21241023, and World Premier International Research Center Initiative (WPI), MEXT, Japan.

Notes and references

1 M. De, P. S. Ghosh and V. M. Rotello, *Adv. Mater.*, 2008, **20**, 4225.
2 Y. Jun, J. H. Lee and J. Cheon, *Angew. Chem., Int. Ed.*, 2008, **47**, 5122.
3 J. Kim, Y. Piao and T. Hyeon, *Chem. Soc. Rev.*, 2009, **38**, 372.
4 V. I. Shubayev, T. R. Piasanic and S. Jin, *Adv. Drug Delivery Rev.*, 2009, **61**, 467.
5 J. Kreuter, *Adv. Drug Delivery Rev.*, 2001, **47**, 65.
6 J. M. Nam, C. S. Thaxton and D. A. Mirkin, *Science*, 2003, **301**, 1884.
7 A. Ito, Y. Kuga, H. Honda, H. Kikkawa, A. Horiuchi, Y. Watanabe and T. Kobayashi, *Cancer Lett.*, 2004, **212**, 167.
8 A. Ito, M. Shinlai, H. Honda and T. Kobayashi, *J. Biosci. Bioeng.*, 2005, **100**, 1.
9 X. Wang, J. Zhuang, Q. Peng and Y. Li, *Nature*, 2005, **437**, 121.
10 J. Park, K. An, Y. Hwang, J. G. Park, H. J. Noh, J. Y. Kim, J. H. Park, N. M. Hwang and T. Hyeon, *Nat. Mater.*, 2004, **3**, 891.
11 T. Tanigchi, K. Nakagawa, T. Watanabe, N. Matsushita and M. Yoshimura, *J. Phys. Chem. C*, 2009, **113**, 839.
12 R. Y. Hong, J. H. Li, H. Z. Li, J. Ding, Y. Zheng and D. G. Wei, *J. Magn. Magn. Mater.*, 2008, **320**, 1605.
13 S. Takami, T. Sato, T. Mousavand, S. Ohara, M. Umetsu and T. Adschiri, *Mater. Lett.*, 2007, **61**, 4769.
14 Y. Zhang, N. Kohler and M. Zhang, *Biomaterials*, 2002, **23**, 1553.
15 M. Taupitz, J. Wagner and J. Schonorr, *Invest. Radiol.*, 2002, **37**, 482.
16 T. Neuberger, B. Schöpf, H. Hofmann, M. Hofmann and B. Rechenberg, *J. Magn. Magn. Mater.*, 2005, **293**, 483.
17 M. S. Nikolic, M. Krack, V. Aleksandrovic, A. Kornowski, S. Förster and H. Weller, *Angew. Chem., Int. Ed.*, 2006, **45**, 6577.
18 A. F. Thünemann, D. Schütt, L. Kaufner, U. Pison and H. Mohwald, *Langmuir*, 2006, **22**, 2351.
19 U. I. Tromsdorf, O. T. Bruns, S. C. Salman, S. C. Beisegel and H. Weller, *Nano Lett.*, 2009, **9**, 4434.
20 S. Peng, C. Wang, J. Xie and S. Sun, *J. Am. Chem. Soc.*, 2006, **128**, 10676.
21 R. Hong, N. O. Fischer, T. Emrich and V. M. Rotello, *Chem. Mater.*, 2005, **17**, 4617.
22 R. Hong, N. O. Fischer, T. Emrick and V. M. Rotello, *Chem. Mater.*, 2005, **17**, 4617.
23 S.-W. Kim, S. Kim, J. B. Tracy, A. Jasanoff and M. G. Bawendi, *J. Am. Chem. Soc.*, 2005, **127**, 4556.
24 F. Hu, K. W. MacRenaris, E. A. Waters, T. Liang, E. A. Schultz-Sikma, A. L. Eckerman and T. J. Meade, *J. Phys. Chem. C*, 2009, **113**, 20855.
25 B.-S. Kim, J.-M. Qiu, J.-P. Wang and T. A. Taton, *Nano Lett.*, 2005, **5**, 1987.
26 Y. Jun, Y.-M. Huh, J.-S. Choi, J.-H. Lee, H.-T. Song, S. Kim, S. Yoon, K. S. Kim and J. S. Shin, *J. Am. Chem. Soc.*, 2005, **127**, 5732.
27 Y.-M. Huh, Y. Jun, H.-T. Song, S. J. Kim, J.-S. Choi, J.-H. Lee, S. Yoon, K. S. Kim, J. S. Shin, J. S. Suh and J. Cheon, *J. Am. Chem. Soc.*, 2005, **127**, 12387.
28 R. E. Bailey and S. Nie, in *The Chemistry of Nanomaterials: Synthesis, Properties and Application*, Wiley-VCH, Weinheim, 2004, p. 450.
29 S. Kim, S. Bok, S. Lee, H. Kim, M. Lee, Y. B. Park and M. S. Choi, *Toxicol. Appl. Pharmacol.*, 2005, **208**, 29.
30 G. F. Goya, T. S. Berquó and F. C. Fonseca, *J. Appl. Phys.*, 2003, **94**, 3520.
31 T. Rajh, L. X. Chen, K. Lukas, T. Liu, M. C. Thurnauer and D. M. Tiede, *J. Phys. Chem. B*, 2002, **106**, 10543.
32 M. J. McWhirter, P. J. Bremer, I. L. Lamont and A. J. McQuilan, *Langmuir*, 2003, **19**, 3575.
33 W. Huang, P. Jiang, C. Wei, D. Zhuang and J. L. Shi, *J. Mater. Res.*, 2008, **23**, 1946.
34 M. J. McWhirter, P. J. Bremer, I. L. Lamont and A. J. McQuillan, *Langmuir*, 2003, **19**, 3575.
35 S. A. Gómez-Lopera, R. C. Plaza and A. V. Delgado, *J. Colloid Interface Sci.*, 2001, **240**, 40.
36 T. Togashi, T. Naka, S. Asahina, K. Sato, S. Takami and T. Adschiri, *Dalton Trans.*, 2011, **40**, 1073.
37 M. Jarlbring, L. Gunneriusson, B. Hussman and W. Forsling, *J. Colloid Interface Sci.*, 2005, **285**, 212.
38 T. Ishimatsu, S. Hirose and H. Sakurai, *Talanta*, 1977, **24**, 555.
39 A. L. Petrou and M. V. Koromantzou, *Transition Met. Chem.*, 1991, **16**, 48.
40 A. L. Petrou, P. Paraskevopoulou and M. Chrysikopoulou, *J. Inorg. Biochem.*, 2004, **98**, 123.
41 R. H. Kodama, *J. Magn. Magn. Mater.*, 1999, **200**, 470.
42 X. Sun, C. Zheng, F. Zhang, Y. Yang, G. Wu, A. Yu and N. Guan, *J. Phys. Chem. C*, 2009, **113**, 16002.
43 P. Guardia, B. Batlle-Brugal, A. G. Roca, O. Iglesias, M. P. Morales, C. S. Serna, A. Labarta and X. Batlle, *J. Magn. Magn. Mater.*, 2007, **316**, e756.
44 K. R. Vega-Villa, J. K. Takemoto, J. A. Yánez, C. M. Remsberg, M. L. Forrest and N. M. Davis, *Adv. Drug Delivery Rev.*, 2008, **60**, 929.
45 S. M. Moghimi, A. C. Hunter and J. C. Murray, *FASEB J.*, 2005, **19**, 311.
46 T. Xia, M. Kovochich, J. Brant, M. Hotze, J. Sempf, T. Oberley, C. Sioutas, J. H. Yeh, M. R. Wiesner and V. F. Nel, *Nano Lett.*, 2006, **6**, 1794.
47 M. A. Dorbovlskaia and S. E. Mcneil, *Nat. Nanotechnol.*, 2007, **2**, 469.

CrystEngComm

Dynamic Article Links

Cite this: *CrystEngComm*, 2012, **14**, 2117

www.rsc.org/crystengcomm

PAPER

Simple and rapid synthesis of ZrO_2 nanoparticles from $Zr(OEt)_4$ and $Zr(OH)_4$ using a hydrothermal method

Minori Taguchi,*[a] Seiichi Takami,[b] Tadafumi Adschiri,[c] Takayuki Nakane,[a] Koichi Sato[a] and Takashi Naka[a]

Received 23rd October 2011, Accepted 8th December 2011
DOI: 10.1039/c2ce06408a

A simple and rapid technique was established for synthesis of ZrO_2 nanoparticles from zirconium ethoxide ($Zr(OEt)_4$) and zirconium hydroxide ($Zr(OH)_4$) as the precursors, using the sub- or supercritical hydrothermal method. The precursors were treated in a batch-type reactor with the reaction temperatures between 200 and 500 °C for 10 min. The products obtained at temperatures higher than 300 °C had mixtures of tetragonal and monoclinic phases. The higher the reaction temperature, the higher the volume fraction of the monoclinic phase. Selection of a suitable precursor is the most important point in this synthesis technique. $Zr(OH)_4$ was found to be a better precursor for obtaining ZrO_2 with a higher volume fraction of monoclinic phase than $Zr(OEt)_4$ under the same synthesis conditions. Single phase pure monoclinic ZrO_2 was successfully obtained after heat treatment at 500 °C. The growth rate of ZrO_2 nanoparticles obtained from $Zr(OEt)_4$ and $Zr(OH)_4$ was different. The products contained some chemisorbed water and/or a hydroxide group on the surface. Their presence was dependent on the reaction temperature and the particle size, and not on the precursor used. However, there was no significant difference among the band gaps of ZrO_2 synthesized from different precursors, confirming that the type of precursor does not affect the quality as much as the crystallinity of the products.

Introduction

Zirconium oxide (ZrO_2) has several crystalline phases, *i.e.*, amorphous, metastable tetragonal, monoclinic, tetragonal, and cubic phases.[1,2] Since each crystalline phase possesses attractive functional properties, ZrO_2 is widely used in a variety of technological fields like fuel cell electrolyte,[3,4] engineering ceramic,[5,6] catalyst or catalyst support,[7,8] oxygen sensor,[9,10] and gate dielectric.[11,12] For these applications, ZrO_2 is fabricated in various forms like single crystal, thin film, nanoparticles, and polycrystalline bulk. The preparation of ZrO_2 nanoparticles applicable to high-surface area catalysts, optical and electronic nanodevices is one of the important and attractive topics of research.[13–16] Controlling the crystalline phase and the particle size is an important issue during its synthesis. For this issue, wet processes, such as solvo- or hydrothermal methods, are generally utilized for synthesis. However, the optimization of the experimental conditions has not been simple.[13–16] Therefore, development of a simple and rapid synthesis method for controlling the crystalline phase and the particle size is still an important and meaningful study from the viewpoint of its industrial application.

Use of sub- or supercritical water in the hydrothermal method is one of the promising approaches for simple and rapid synthesis of metal oxide nanoparticles.[17–21] The heating of water in a sealed vessel decreases the dielectric constant drastically at around the critical point, resulting in drastic change in the solubility of inorganic substances in it.[22,23] This phenomenon is useful for faster nucleation and crystal growth of the metal oxides. In addition, organic molecules, dissolved under these conditions, can modify the surface of the metal oxide nanoparticle during the hydrothermal method utilizing sub- or supercritical water. Employing this method, previously we succeeded in synthesizing not only simple metal oxides, but also surface-modified metal oxide nanoparticles.[17–21]

With this background, we tried to synthesize ZrO_2 nanoparticles in a flow-type reactor using the supercritical hydrothermal method.[21] The selection of the starting precursor is an especially important point because it affects the nucleation and/or the growth rates of the crystal, the purity, the crystallinity, and the phase stability of the products. As an example, metal halides, nitrates, and sulfates are common starting inorganic substances of the hydrothermal method, but they cannot be used directly as precursors because the reactor is corroded by the counter anions. To reduce the contamination owing to this corrosion as much as possible, we focused on using zirconium ethoxide ($Zr(OEt)_4$) and zirconium hydroxide ($Zr(OH_4)$) as the precursors because they were expected to prevent the corrosion by their counter anions. The quality of the products was discussed from the viewpoint of their structure and optical characteristics.

[a]*National Institute for Materials Science, 1-2-1 Sengen, Tsukuba, 305-0047, Japan*
[b]*Institute of Multidisciplinary Research for Advanced Materials, Tohoku University, 2-1-1 Katahira, Aoba-ku, Sendai, 980-8577, Japan*
[c]*WPI, Advanced Institute for Materials Research, Tohoku University, 2-1-1 Katahira, Aoba-ku, Sendai, 980-8577, Japan*

Experimental

Materials

Zirconium ethoxide (98%, $Zr(OEt)_4$) and zirconium hydroxide (97%, $Zr(OH)_4$) used as precursors of the hydrothermal method in this study were purchased from Wako Chemicals and Aldrich, respectively.

Sample preparation

Each precursor (with concentrations of 0.10 M) and distilled water were transferred to a pressure-resistant Hastelloy C vessel (inner volume: 5.0 mL). A hydrothermal reaction was performed using an electric furnace at appropriate temperatures ranging from 200 to 500 °C, heated in increments of 100 °C, for 10 min. The inner pressure of the reactor was controlled and maintained at 38 MPa for all the samples. The amount of the distilled water weighted was 4.5 g at 200 °C, 3.8 g at 300 °C, 2.5 g at 400 °C, or 0.8 g at 500 °C. The reaction vessel was then quenched by submerging it into a water bath at room temperature. After the reaction, solid products were washed by a combination of repeated centrifugation and decantation, alternately with water and methanol. Finally, the products were dried in air at room temperature. Hereafter, these products are designated as **OEt-200** (from $Zr(OEt)_4$ at 200 °C), **OEt-300** (from $Zr(OEt)_4$ at 300 °C), **OEt-400** (from $Zr(OEt)_4$ at 400 °C), **OEt-500** (from $Zr(OEt)_4$ at 500 °C), **OH-200** (from $Zr(OH)_4$ at 200 °C), **OH-300** (from $Zr(OH)_4$ at 300 °C), **OH-400** (from $Zr(OH)_4$ at 400 °C), and **OH-500** (from $Zr(OH)_4$ at 500 °C).

Characterizations

X-Ray diffraction (XRD) patterns of the products were recorded using a RINT-2000 diffractometer (Rigaku) with Cu Kα (λ = 1.542 Å) radiation at a 2θ scan speed of 2° min^{-1}. To estimate the volume fractions of monoclinic and tetragonal phases present in each product, we calculated the ratio of the intensities of the ($\bar{1}11$) and the (111) peaks for the monoclinic, and of the (101) peak for the tetragonal phases using eqn (1)–(3) as follows:[24]

$$X_m = (I_m(\bar{1}11) + I_m(111))/(I_m(\bar{1}11) + I_m(111) + I_t(101)) \quad (1)$$

$$v_m = (1.311X_m)/(1 + 0.311X_m) \quad (2)$$

$$v_t = 1 - v_m \quad (3)$$

In the above equations, X_m is an intensity ratio of the monoclinic and the tetragonal phases; $I_m(\bar{1}11)$ and $I_m(111)$ are the intensities of the ($\bar{1}11$) and the (111) peaks for the monoclinic phase, respectively; $I_t(101)$ is the intensity of the (101) peak for the tetragonal phase; and v_m and v_t are the volume fractions of the monoclinic and the tetragonal phases, respectively. The lattice parameters were calculated from the XRD patterns of the products using a unit cell parameter refinement program (Cell Calc).[25] The Scherrer equation was used to determine the crystallite size of the products from the full width at half maximum (FWHM) of the monoclinic ($\bar{1}11$) peak or tetragonal (101) peak, and a shape factor of 0.9. A transmission electron microscope (TEM, JEM-1200EX, JEOL) was used to obtain the magnified image of the products. The arithmetic mean particle diameter and the size distribution of the products were estimated from the TEM images. Additionally, the volume weighted average of the particle diameter was also calculated from the arithmetic mean particle diameter of the products.[18]

Fourier transform infrared (FT-IR) spectra were recorded using an FT/IR-6200 Plus (JASCO) with KBr pellets. UV-Vis powder diffuse reflectance spectra were recorded using a V-650 spectrophotometer (JASCO). The obtained spectra were converted to the absorption spectra using the Kubelka–Munk calculation.[26]

$$(1 - R_\infty)^2/2R_\infty = F(R_\infty) = K/S \quad (4)$$

$$R_\infty = R_{sample}/R_{reference} \quad (5)$$

In the above equations, R_∞ is the relative reflectance of the sample (R_{sample}) and reference ($R_{reference}$); K and S are absorption and scattering coefficients of the sample, respectively; and $F(R_\infty)$ is the Kubelka–Munk function.

Results and discussion

Fig. 1 shows the XRD patterns of the ZrO_2 nanoparticles produced using the sub- or supercritical hydrothermal method. The pattern of **OEt-200** shows some weak peaks, which can be assigned as the tetragonal phase (JCPDS no. 80-0965) of ZrO_2; the pattern of **OH-200** shows an amorphous pattern similar to the untreated $Zr(OH)_4$. **OEt-300–500** and **OH-300–400** obviously had both tetragonal and monoclinic (JCPDS no. 83-0944) phases. **OH-500** was almost a single phase of monoclinic structure. These results suggest that our synthesis technique utilizing sub- or supercritical water in the hydrothermal method is simple without any special reagents, and that it is effective to produce ZrO_2 in a quite short reaction time of only 10 min. The volume fraction of the crystalline phase, the lattice parameters, and the crystallite size of the products are summarized in Table 1. A systematic change was not seen in the lattice parameters of the monoclinic ZrO_2 in the products. Therefore, the quality of the product in terms of the crystallinity of the monoclinic ZrO_2

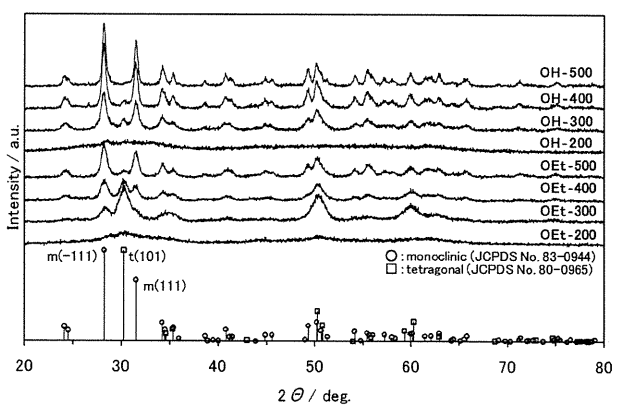

Fig. 1 XRD patterns of the products synthesized from $Zr(OEt)_4$ at 200 °C (**OEt-200**); 300 °C (**OEt-300**); 400 °C (**OEt-400**) and 500 °C (**OEt-500**), synthesized from $Zr(OH)_4$ at 200 °C (**OH-200**); 300 °C (**OH-300**); 400 °C (**OH-400**) and 500 °C (**OH-500**) and JCPDS Card no. 83-0944 as (circle) monoclinic ZrO_2 and 80-0965 as (square) tetragonal ZrO_2.

seems to be independent of the precursor, even though the difference in crystallite size between the products is apparent. The crystallite size was larger for the products synthesized at higher reaction temperatures for both the precursors. However, the crystallite sizes of the products synthesized from $Zr(OEt)_4$ (**OEt**-series) were smaller than those synthesized from $Zr(OH)_4$ (**OH**-series). This difference was verified by TEM observation too.

The TEM images, the arithmetic mean particle diameters, and the size distributions of the products are shown in Fig. 2. The volume weighted averages of the particle diameters are shown in Table 1. The obtained particle sizes were close to the crystallite sizes calculated from the XRD patterns. Moreover, the dependence of the particle size on the reaction temperature and the precursor appears to be similar to the results obtained from the XRD data. Fig. 2 also shows that the reaction temperature affects not only the particle size, but also the morphology. The morphologies of **OEt-** and **OH-300–500** showed a spherical shape; however, some particles of **OEt-500** and **OH-400–500** with relatively larger particle size showed distorted spherical shape. Although fine particles below 5 nm were confirmed in **OEt-200**, an accurate particle size could not be estimated. **OH-200** was also insufficient for the formation of the nanostructures with definite size and morphology. Meanwhile, the size distributions of **OEt-300–500** look narrower than that of **OH-300–500**. It seems that the larger the particle size, the wider the size distribution. **OH-400** and **OH-500** with relatively large particles prominently showed the wide size distribution.

On the other hand, the volume fraction of the monoclinic phase depends on the reaction temperature. The higher the reaction temperature, the higher the volume fraction of the monoclinic phase. Moreover, it does not depend only on the reaction temperature but also on the precursor. For increasing the volume fraction of the monoclinic phase, $Zr(OH)_4$ was found to be a better precursor than $Zr(OEt)_4$ for rapid synthesis of monoclinic ZrO_2. Both the particle (crystallite) size and the volume fraction of **OH**-series are larger than those of **OEt**-ones for the same reaction temperature. Fig. 3 plots the volume fraction of the monoclinic phase and the particle size (D_{TEM}) against the reaction temperature for **OEt-** and **OH-300–500**. Remarkably, both the volume fractions of the crystalline phase and the particle size depended on the precursor.

To understand these precursor-dependent phenomena, our results were compared with the previous reports about the crystallization from the precursor to ZrO_2 under hydrothermal conditions.[27–30] In the previous reports, when the zirconia precursor was treated under hydrothermal conditions, the product ZrO_2 contained mixtures of tetragonal and monoclinic phases.[27–29] The volume fraction of the monoclinic phase in the product ZrO_2 depended on the pH controlled using alkaline agents or premixed mineralizes of the starting water. These reports suggest that the coexisting ions or substances in the water play an important role in controlling the phase contents of the product ZrO_2. In particular, they affect the solubility of the precursor. When the solubility of the precursor is high in the solution, an increase in the volume fraction of the monoclinic phase in the product ZrO_2 is shown.[29] This study added neither alkaline agents nor other reagents for pH control; however, the counter anion of the precursor was thought to influence the reaction route of the crystalline phase of ZrO_2. For example, the counter anions OEt^- ($Zr(OEt)_4$) and OH^- ($Zr(OH)_4$) are likely to affect the pH under these conditions. Indeed, the basicity or acidity between OEt^- and OH^- is different.[31] Therefore, there is a possibility that the difference in the counter anions of the precursors contributes to the precursor-dependent phenomena. That is, they affect the pH and thus change the solubility of the precursor. In that case, the solubility of zirconium hydroxide as the precursor should be taken into account, because the state of the hydroxides depends on the pH of the solution.[32–35] It means that the presence of the counter anions is thought to influence the state of the hydroxides formed during the reaction. The state of the hydroxides is not simple; however, it seems to be concerned with the relationship between the pH of the solution and the solubility of the hydroxide. On the other

Table 1 Volume fraction ratio of monoclinic and tetragonal phases, lattice parameters and particle sizes from the XRD (D_{XRD}) and TEM (D_{TEM}) results of the products

Products	Volume fraction ratio of monoclinic and tetragonal phase ν_m/ν_t (%)[a]		Lattice parameters					Particle size/nm		
								D_{XRD}		
			a/Å	b/Å	c/Å	β/deg	V/Z/Å^3	m[a]	t[a]	D_{TEM}
OEt-200	—	t	3.582(8)	—	5.21(2)	—	33.47	—	—	—
OEt-300	50/50	t	3.591(5)	—	5.19(2)	—	33.49	12.6	12.4	9.3
		m	5.151(3)	5.189(5)	5.308(6)	98.58	35.08			
OEt-400	75/25	m	5.155(3)	5.214(2)	5.305(4)	99.11	35.21	18.0	16.0	15.6
OEt-500	91/9	m	5.156(2)	5.213(3)	5.323(3)	99.18	35.32	25.9	—	19.4
OH-200	—	—	—	—	—	—	—	—	—	—
OH-300	89/11	m	5.158(3)	5.208(5)	5.319(4)	99.24	35.26	24.8	—	15.1
OH-400	94/6	m	5.154(2)	5.210(2)	5.322(2)	99.30	35.27	37.6	—	30.2
OH-500	97/3	m	5.151(2)	5.207(2)	5.314(2)	99.28	35.17	39.7	—	35.8
JCPDS 80-0965	0/100	t	3.5920	—	5.1830	—	33.45	—	—	—
JCPDS 83-0944	100/0	m	5.1423	5.2000	5.3110	99.205	35.05	—	—	—

[a] The m and t represent monoclinic and tetragonal phases, respectively. The line (—) indicates the uncalculated values because of the small XRD peaks, unclear TEM images, and JCPDS cards.

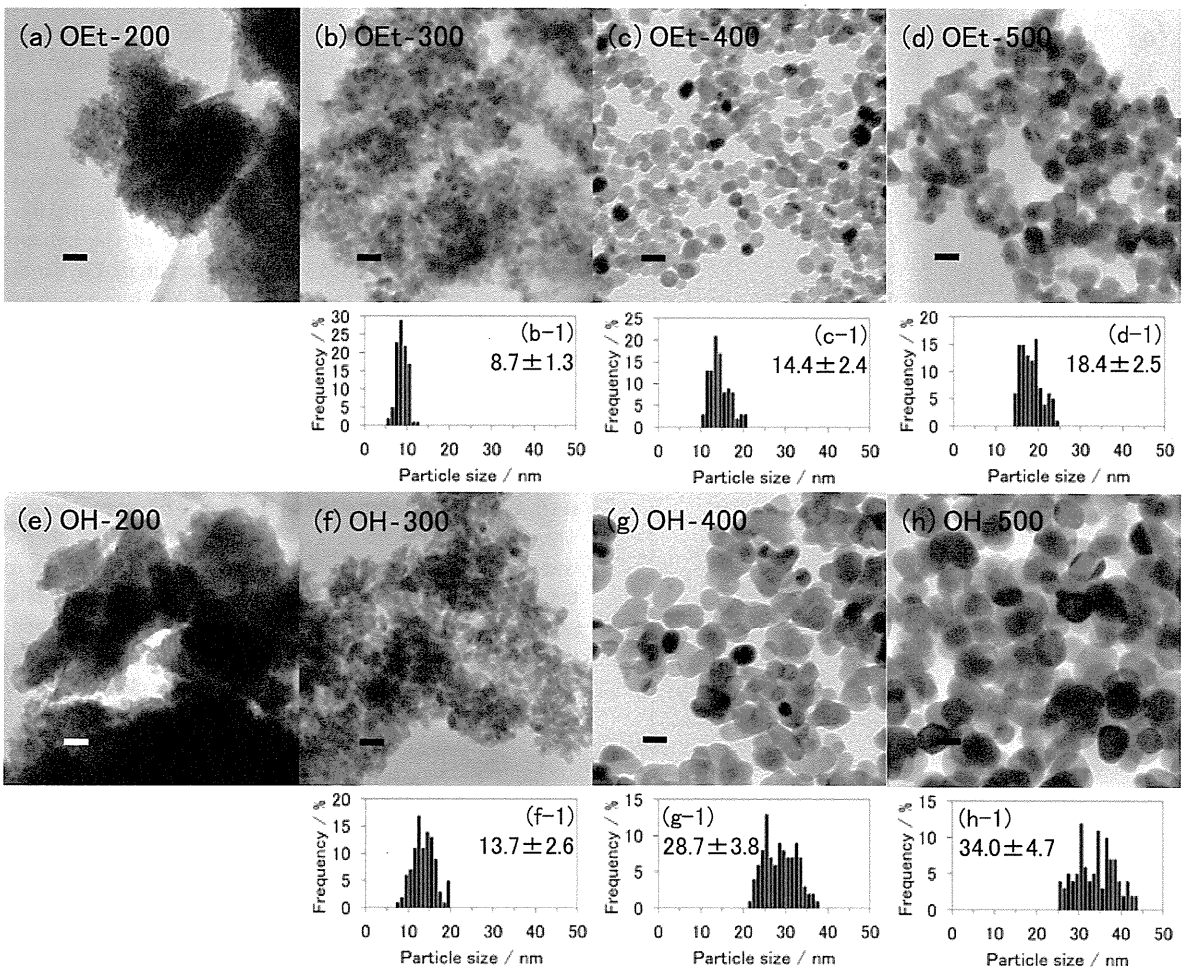

Fig. 2 TEM images of the products synthesized from $Zr(OEt)_4$ at (a) 200 °C (**OEt-200**); (b) 300 °C (**OEt-300**); (c) 400 °C (**OEt-400**) and (d) 500 °C (**OEt-500**), synthesized from $Zr(OH)_4$ at (e) 200 °C (**OH-200**); (f) 300 °C (**OH-300**); (g) 400 °C (**OH-400**) and (h) 500 °C (**OH-500**); scale bar = 20 nm. The particle size distribution histograms and the arithmetic mean particle diameters of (b-1) **OEt-300**; (c-1) **OEt-400**; (d-1) **OEt-500**; (f-1) **OH-300**; (g-1) **OH-400** and (h-1) **OH-500**.

hand, the reaction temperature also affects the solubility of the precursor because the dielectric constant of water changes with temperature.[22,23] The solubility of inorganic substances becomes low around the critical point and is dependent on the counter anion. The volume fraction of the monoclinic phase in the products was higher for **OH-300** than that of **OEt-300**, suggesting that the solubility of $Zr(OH)_4$ is higher than that of $Zr(OEt)_4$ under the same conditions. These reports also suggest that the pH plays an important role in the volume fraction of the crystalline phase in the product ZrO_2.

Moreover, the relationship between the results of Fig. 3 and the difference in the counter anions should be discussed not only from the pH of the solution but also from the phase transition rate from tetragonal to monoclinic phases. The amount of the monoclinic phase in **OH**-series was larger than that in **OEt**-ones. Hence, the rate of **OH**-series should be faster than that of **OEt**-ones. The previous studies showed that the transition rate correlates with the surface condition of the product ZrO_2.[36,37] In particular, the rate is controlled and accelerated by the adsorption of water (H_2O) and/or hydroxide ion (OH^-) on the surface. They reported that the phase transition of ZrO_2 from tetragonal to monoclinic occurs at the surface under hydrothermal conditions. Therefore, the difference in the counter anions also seems to change the transition rate between **OEt**- and **OH**-series in the case of the present study. Notably, the fast rate of **OH**-series is attributed to OH^-. According to Garvi,[38] smaller grains can stabilize ZrO_2 to the tetragonal phase because the surface energy of this phase is much less than that of the monoclinic phase. The particle size of the products was larger for the **OH**-series than that of the **OEt**-ones under the same conditions. The difference in growth rate of the phases was considered as the reason for the different volume fraction of the monoclinic phase in the product. In summary, it is clear that the crystalline phase and the particle size of the product ZrO_2 can be controlled by the selection of a suitable precursor and tuning of the reaction temperature.

As the next step, optical characteristics of the products were investigated in order to verify the influence of the hydrothermal method using different precursors on the quality of the nanosized products. Fig. 4 shows the FT-IR spectra of all the products. In general, the Zr–O bands in the ZrO_2 crystal appear at the region